Check for updates

View Article Online
View Journal

Dalton Transactions

An international journal of inorganic chemistry

Accepted Manuscript

This article can be cited before page numbers have been issued, to do this please use: J. Satra, U. K. Ghorui, P. Mondal, G. R. Bhadu and B. Adhikary, *Dalton Trans.*, 2020, DOI: 10.1039/D0DT01012J.

This is an Accepted Manuscript, which has been through the Royal Society of Chemistry peer review process and has been accepted for publication.

Accepted Manuscripts are published online shortly after acceptance, before technical editing, formatting and proof reading. Using this free service, authors can make their results available to the community, in citable form, before we publish the edited article. We will replace this Accepted Manuscript with the edited and formatted Advance Article as soon as it is available.

You can find more information about Accepted Manuscripts in the Information for Authors.

Please note that technical editing may introduce minor changes to the text and/or graphics, which may alter content. The journal's standard Terms & Conditions and the Ethical guidelines still apply. In no event shall the Royal Society of Chemistry be held responsible for any errors or omissions in this Accepted Manuscript or any consequences arising from the use of any information it contains.

ROYAL SOCIETY OF CHEMISTRY

rsc.li/dalton

View Article Online
DOI: 10.1039/D0DT01012J

One pot solvent assisted syntheses of Ag_3SbS_3 nanocrystals and exploring their phase dependent electrochemical behavior toward oxygen reduction reaction and visible light induced methanol oxidation reaction

Jit Satra,[a] Uday Kumar Ghorui,[a] Papri Mondal,[a] Gopala Ram Bhadu,[b] Bibhutosh Adhikary*[a]

* Corresponding authors

[a] Department of Chemistry, Indian Institute of Engineering Science and Technology, Shibpur, Howrah 711 103, West Bengal, India

Email: bibhutosh@chem.iiests.ac.in

[b] Department of Analytical and Environmental Science Division and Centralized Instrument Facility, Gijubhai Badheka Marg, Bhavnagar 364021, Gujarat, India

Published on 05 June 2020. Downloaded by University of Exeter on 6/9/2020 8:08:14 PM.

Dalton Transactions Accepted Manuscript

View Article Online
DOI: 10.1039/D0DT01012J

Published on 05 June 2020. Downloaded by University of Exeter on 6/9/2020 8:08:14 PM.

Dalton Transactions Accepted Manuscript

Abstract

A huge variety of silver based ternary sulfide semiconductors (SCs) have been considered for the sustainable advancement of renewable energy source. Herein, we have synthesized two important classes of newly emerging semiconductor nanocrystal (NC) Ag_3SbS_3 (SAS) i.e. hexagonal and monoclinic by simply tuning the solvent polarity, of which the second one have been synthesized in a phase pure NC for the first time by the thermal decomposition of silver and antimony based dithiocarbamate ($\sim$N-CS_2-M) complexes. Interestingly, these two systems exhibit two different semiconducting (SC) properties and band gaps; hexagonal SAS has p type (E_g~1.65 eV) whereas monoclinic SAS has n type (E_g~2.1 eV) character. For the first time ever we have designed a reducing working electrode (i.e. cathode) by modifying rotating disc electrode (RDE) with hexagonal SAS which exhibits excellent electrochemical oxygen reduction reaction (ORR) activity (E_{onset}=1.09 V Vs. RHE and average number of electron transfer: 3.89) comparable to the highly expensive Pt/C (E_{onset}=0.88 V Vs. RHE and average number of electron transfer: 3.92). Density Functional Theory (DFT) investigation confirms the corroborations of experimental data with theoretical implications. In addition, the electrode fabricated by monoclinic SAS acts as an efficient photoanode which performs higher photoelectrochemical (PEC) methanol oxidation reaction (MOR) activity under illumination in alkaline medium compared to standard TiO_2 grown on indium tin oxide (ITO) coated glass slide. On illumination the relative photocurrent density at onset potential has been obtained to be 845 which is a very significant experimental output with respect to any other TiO_2 or Pt@TiO_2 based photocatalyst for this application. The physiochemical stability and reusability of both materials were supported by fifty hours of extended electrochemical chronoamperometric measurements and powder XRD, TEM analyses after electrocatalysis. This study explores a possible pathway for

View Article Online
DOI: 10.1039/D0DT01012J

Published on 05 June 2020. Downloaded by University of Exeter on 6/9/2020 8:08:14 PM.

Dalton Transactions Accepted Manuscript

designing a simple and less expensive but catalytically efficient silver based ternary sulfide NC systems for developing an SC material to reduce the energy crisis in near future.

Introduction

Designing efficient, low cost and stable hybrid catalysts is vital for the development of futuristic fuel cells. In this context cathodic electrochemical oxygen reduction reaction (ORR) and anodic photo oxidation of alcohol as fuel are two critical reactions that explore the conclusive efficiency of a fuel cell in terms of low over potential and high output of energy.[1-12] In case of ORR, Platinum (Pt) has been widely used as a preferred electrocatalyst in a liquid feed fuel cell (LFFC).[13-14] Although ultrafine Pt nanoaparticles having higher surface energies leads to fast aggregation that suffers from poor reduction, retard kinetics and instability of the catalysts.[15-17] Most importantly the very high cost of Pt based electrocatalyst has a negative impact on commercializing fuel cells. But, there was always an urge to replace Pt with an efficient alternative candidate cheaper than it. Therefore vast researches are going on with an aim to reduce the use of platinum in catalytic processes without losing their activity and stability. Very recently two dimensional, three dimensional binary and ternary metal chalcogenides like WSe_2, CoS_2, MoS_2, $MoSe_2$, $NiCo_2S_4$, $FeNiS_2$, $CuCoS_4$, $CoInS_4$ etc. have attracted more attention due to their electrochemical properties having facile synthetic procedure, active surface edges, basal planes, high surface area and especially low cost.[18-28] Not only that, mixed valence metal sulfides have shown notable stability in aqueous alkaline medium and better redox chemistry than metal oxides. We must consider that ternary sulfide has higher redox reaction sites than binary due to its closely packed array of S^{2-} throughout crystal structure.[29-31]On the other hand photoelectrochemical (PEC) organic substrate oxidation reaction leads to hydrogen generation

View Article Online
DOI: 10.1039/D0DT01012J

Published on 05 June 2020. Downloaded by University of Exeter on 6/9/2020 8:08:14 PM.

Dalton Transactions Accepted Manuscript

through water splitting. For example PEC methanol oxidation reaction (MOR) can replace water oxidation for source of electrons to reduce proton ($2H^+ + 2e = H_2$) as it inhibits kinetic limitations for water oxidation. However it has been challenging to carry out MOR by photogenerated charge carriers in terms of activity and stability. MOR studies on widely used semiconductor TiO_2 have indicated methanol adsorption process followed by the formation of a CH_3O• radical and its subsequent oxidation with a valence band hole.[32-34] As TiO_2 has a large band gap, it has been considered to be a poor solar absorber as it shows photocurrent density less than 1 mA. Though many efforts have been done by coupling TiO_2 with noble metal such as Pt to optimize the enhancement of photocurrent density but it remains a challenge to develop such semiconductor having convenient band diagram aligned with the redox potential of the desired PEC reaction and stability. Ag_3SbS_3 (SAS) is a newly emerging class of semiconductor due to its narrow band gap and high surface area. SAS has already been used in the field of nonlinear optics, piezoelectricity, silver ion conductor, solar absorber and photocatalyst for dye degradation.[35-44] Recently, Huang et al. have studied morphology tunable growth of SAS nanocrystal (NC) by changing solvent polarity and its facet dependent application in PEC water splitting reaction as well as in photovoltaic field.[44] On the other hand Wang et al in one of their pioneering work had explored a single source precursor approach for synthesizing copper antimony sulfide with different band gap on changing ligand molecule.[45] Further, Sb belongs to heavy metal elements that does not react with any species suspended in water and form compound so it has been convenient for us to make use of SAS in aqueous electrolytic solution.[41] Moreover, for many applications surface functionalization of NC has been done to improve electrochemical conductivity as shorter ligands may alter the electronic properties by forming active centers on the surface and ease the redox process.[46,47]

View Article Online
DOI: 10.1039/D0DT01012J

Published on 05 June 2020. Downloaded by University of Exeter on 6/9/2020 8:08:14 PM.

Dalton Transactions Accepted Manuscript

Here we report for the first time a unique synthetic procedure to develop SAS based electrocatalyst for ORR and photo induced MOR separately. By simply tuning solvent polarity, we have synthesized the same stoichiometric composition of SAS nanomaterial but different crystal systems (hexagonal and monoclinic) and semiconducting (SC) properties (p type and n type). We have explained the whole ORR catalytic process by hexagonal SAS with the thermodynamical approach by density functional theory (DFT) calculations. By comparing with commercial Pt/C we have found that our material is slightly superior in terms of onset, half wave potential, mass activity and durability than Pt/C. Beside this, we have also focused on MOR as a model alcohol oxidation reaction on the surface of superior monoclinic SAS (n type) NC over TiO_2 under visible light illumination. Due to low band gap, high charge carrier density and surface functionalized active sites of SAS, diffusion of methanol into catalytic interface and subsequently oxidation could occur at as low as 20 mM concentration of methanol. This study might open a strategy in developing semiconductor NC that can replace expensive metal catalysts for ORR and MOR in fuel cell.

Experimental section

Chemicals and Experimental Methods

Details of materials, physical measurements, device fabrication for PEC-MOR, ORR and electrochemical characterization for both ORR and PEC MOR have been illustrated in supporting information. Triethyl ammonium salt of piperidinedithio carbamate ligand ($C_5H_{10}NC\{S\}S^-Et_3NH^+$) (Pip-dtc), Ag(Pip-dtc) and Sb(Pip-dtc)$_3$ complex have been prepared by previously reported method.[48-50]

View Article Online
DOI: 10.1039/D0DT01012J

Published on 05 June 2020. Downloaded by University of Exeter on 6/9/2020 8:08:14 PM.

Dalton Transactions Accepted Manuscript

Syntheses of SAS NCs from precursor complexes

Hexagonal SAS NCs

Here 1 mmol each Ag(Pip-dtc) (white) and Sb(Pip-dtc)$_3$ (pale yellow) was added to a mixture of 20 mL (60 mmol) of OAm and 30 ml (125 mmol) of Dodecanethiol (DDT) (OAm/DDT=1/1.5) in a two necked 100 ml RB flask. To homogenize, the mixture was ultrasonicated for 30 minutes. Then it was heated to 100 ^{0}C for 15 minutes to degas by vacuum pump followed by heated to 220 ^{0}C under argon insertion. During the temperature change from 100 ^{0}C to 200 ^{0}C a distinct colour transformation of reaction mixture was noticed as very pale yellow complex mixture turned into dark brown followed by reddish brown (Fig. 1). The mixture was then annealed at 220 ^{0}C at inert atmosphere for 1h. Then the reaction was cooled to room temperature and stirring was still continued for another 30 minutes. Nanoparticles were precipitated by adding excess anhydrous ethanol. The resulting solution was centrifuged (10000 RPM) to separate the product. The nanoparticles were further dispersed in toluene to remove attached impurities and then it was re-precipitated by excess ethanol. This purification process was repeated 5 times to get the pure desired product.

Monoclinic SAS NCs

1 mmol each Ag(Pip-dtc) and Sb(Pip-dtc)$_3$ were loaded in a two necked 100 ml round bottom (RB) flask in which only 50 ml (150 mmol) of oleylamine (OAm) is added. Here the colour change follows; very pale yellowish mixture to deep orange and finally reddish orange between 100 ^{0}C to 200 ^{0}C (Fig.1). In this preparation, the remaining reaction as well as purification procedure was same as mentioned above.

View Article Online
DOI: 10.1039/D0DT01012J

Published on 05 June 2020. Downloaded by University of Exeter on 6/9/2020 8:08:14 PM.

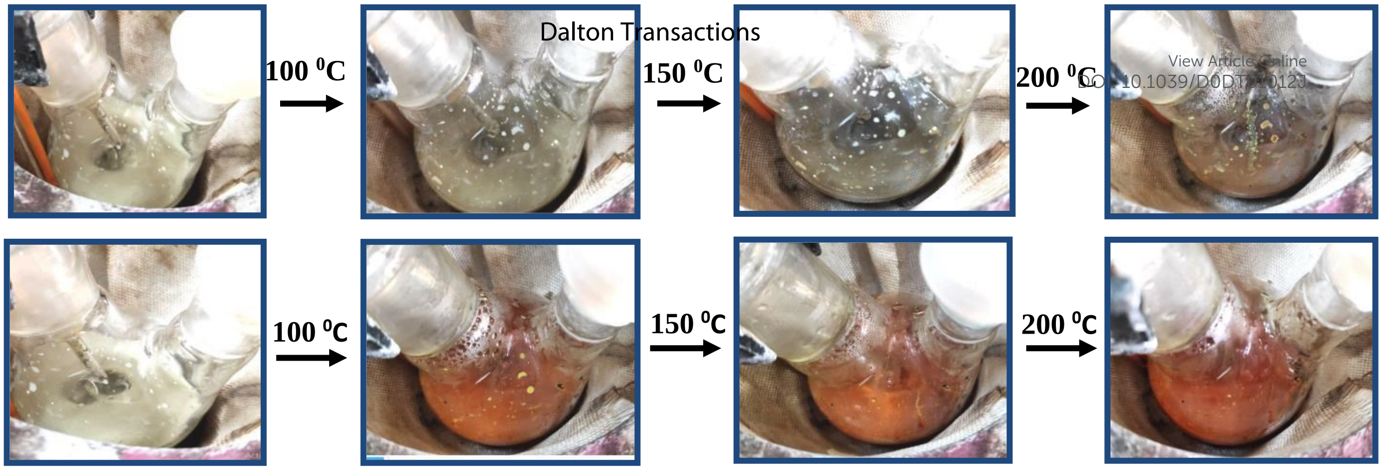

Fig. 1. Colour change during the course of reaction for hexagonal(above) and monoclinic(below).

To study the intrinsic electronic property of the as synthesized NCs in aqueous solution we have carried out a ligand exchange reaction. At first, 1.0 g of $Na_2S{\cdot}9H_2O$ was dissolved in 50 ml of dimethyl formamide (DMF) solvent and then 100 mg of each NC was dispersed in 100 ml toluene by ultrasonication. Each time 10 ml of DMF solution was added into organic ligand toluene solution in every 15 minutes interval and this mixture was kept under ultrasonicated for 5h under room temperature. At last the NCs were purified by centrifugation in toluene followed by ethanol and the process was repeated 5 times. During the course of ligand exchange the colour of the dispersed solution was changed from dark brown to black.

3. Results and discussion

The phase pure structure of two different crystalline systems of SAS has been characterized by powder X-Ray diffraction (XRD) measurement. Fig. 2. (a) and (b) demonstrate the entire sharp and distinct diffraction peaks of the two different SAS (NCs) which has been confirmed by the following; (a) JCPDS NO. 21-1173 (for hexagonal) and (b) JCPDS NO. 25-1187 (for monoclinic). The space group for the hexagonal phase is assigned to R3c(161) and for monoclinic phase is $P2_1/c$(14). The 012 plane for the hexagonal SAS is further designated to SAED pattern (Fig. 3d) where as for the monoclinic SAS NCs, the 130 plane is appeared at the

Dalton Transactions Accepted Manuscript

View Article Online
DOI: 10.1039/D0DT01012J

Published on 05 June 2020. Downloaded by University of Exeter on 6/9/2020 8:07:14 PM.

Dalton Transactions Accepted Manuscript

SAED pattern (Fig. 3j). The phase purity for both the samples has been confirmed by the observation that no other characteristic peaks of Ag_2S, $AgSbS_2$ and Sb_2S_3 have appeared on diffraction patterns.

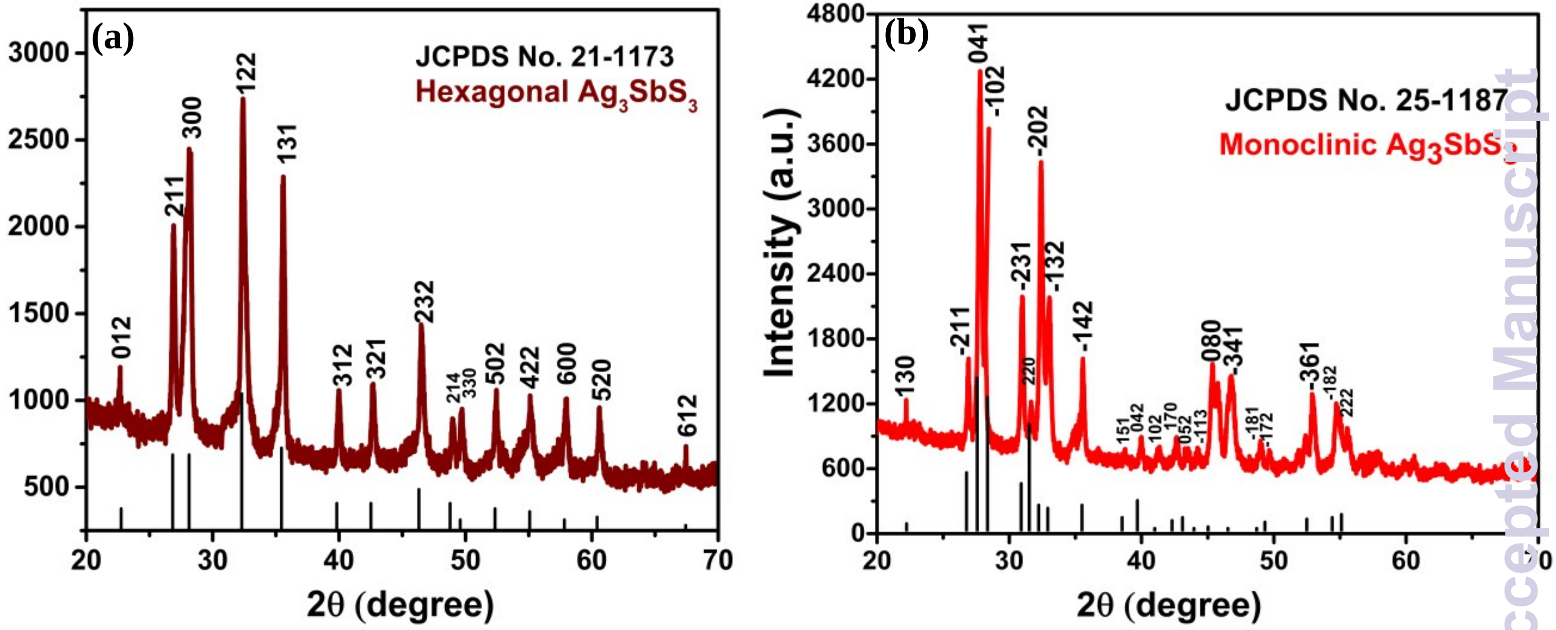

Fig. 2. Powder X-ray diffraction pattern of (a) Hexagonal and (b) Monoclinic.

Stoichiometric composition and elemental mapping of both phases are determined by Electron Dispersive X-ray Analysis (EDX) (Fig. S2). EDX spectra and stoichiometric composition are shown in Fig. S2. (a) hexagonal (b) monoclinic SAS. Elemental mapping for Ag, Sb and S of hexagonal SAS is shown in Fig. S2. (c), (d) and (e) and of monoclinic SAS in Fig. S2. (f), (g) and (h). This study confirms the composition and morphology.

Transmission Electron Microscopic (TEM) and Scanning Electron Microscopic (SEM) images of hexagonal and monoclinic SAS are shown in Fig. 3. TEM images reveal the high crystallinity and phase purity having continuous lattice fringes for both the hexagonal prism and monoclinic ortho-prism like particle. Fig. 3(a) shows low magnification TEM images for hexagonal prismatic particle and the inset shows particle size distribution (on Gaussian fitting) that reveals

View Article Online
DOI: 10.1039/D0DT01012J

Published on 05 June 2020. Downloaded by University of Exeter on 6/9/2020 8:08:14 PM.

Dalton Transactions Accepted Manuscript

the average diameter for the hexagonal prismatic particle is about 100 ± 4 nm. Fig. 3(b) shows the high magnification image of the particle having clearly visible lattice fringes on it. HRTEM image of Fig. 3(c) shows inter planar spacing obtained from fringe pattern which is 0.396 nm (for 012), completely consistent with the standard value of 'd' spacing for the corresponding JCPDS 21-1173. Fig. 3(d) illustrates the SAED pattern for the corresponding 012 plane. SEM image (Fig. 3e) confirms the shape and morphology obtained from TEM i.e. the hexagonal prismatic like particle assigning the characteristic planes (inset). The possible atomic arrangement and the position of crystalline plane (012) in unit cell have been manifested in Fig. 3(f). Similarly Fig. 3(g) shows the particle distribution of monoclinic SAS in low magnification. The size distribution of the monoclinic SAS particle has been represented by the Gaussian plot at inset of Fig. 3(g). As the rod shaped particles have also a 2D facet, so we had to calculate the length along with breadth to explore the size distribution and on doing so we got two distribution histograms. For the length and breadth the average sizes are ~550 ± 5 nm (inset of Fig. 3g) and 142 ± 2 nm (inset of Fig. 3h) respectively. HRTEM image (Fig. 3i) clearly shows the inter-planar distance for monoclinic SAS is 0.398 nm (for 130) that are again consistent with the corresponding JCPDS 25-1187. Fig. 3(j) represents the SAED pattern of the NC indicating the characteristic crystalline plane (130). The SEM image for the monoclinic NC (Fig. 3k) confirms the orthoprismatic morphology of particle. Further the structure of unit cell (Fig. 3l) having crystalline plane (130) has been obtained by combining idea from XRD, TEM and SEM experiments as earlier. The well-defined crystalline shape and morphology of SAS has been obtained by changing polarity and composition of solvent (Scheme 1) as obtained from XRD, TEM and SEM results.

View Article Online
DOI: 10.1039/D0DT01012J

Published on 05 June 2020. Downloaded by University of Exeter on 6/9/2020 8:08:14 PM.

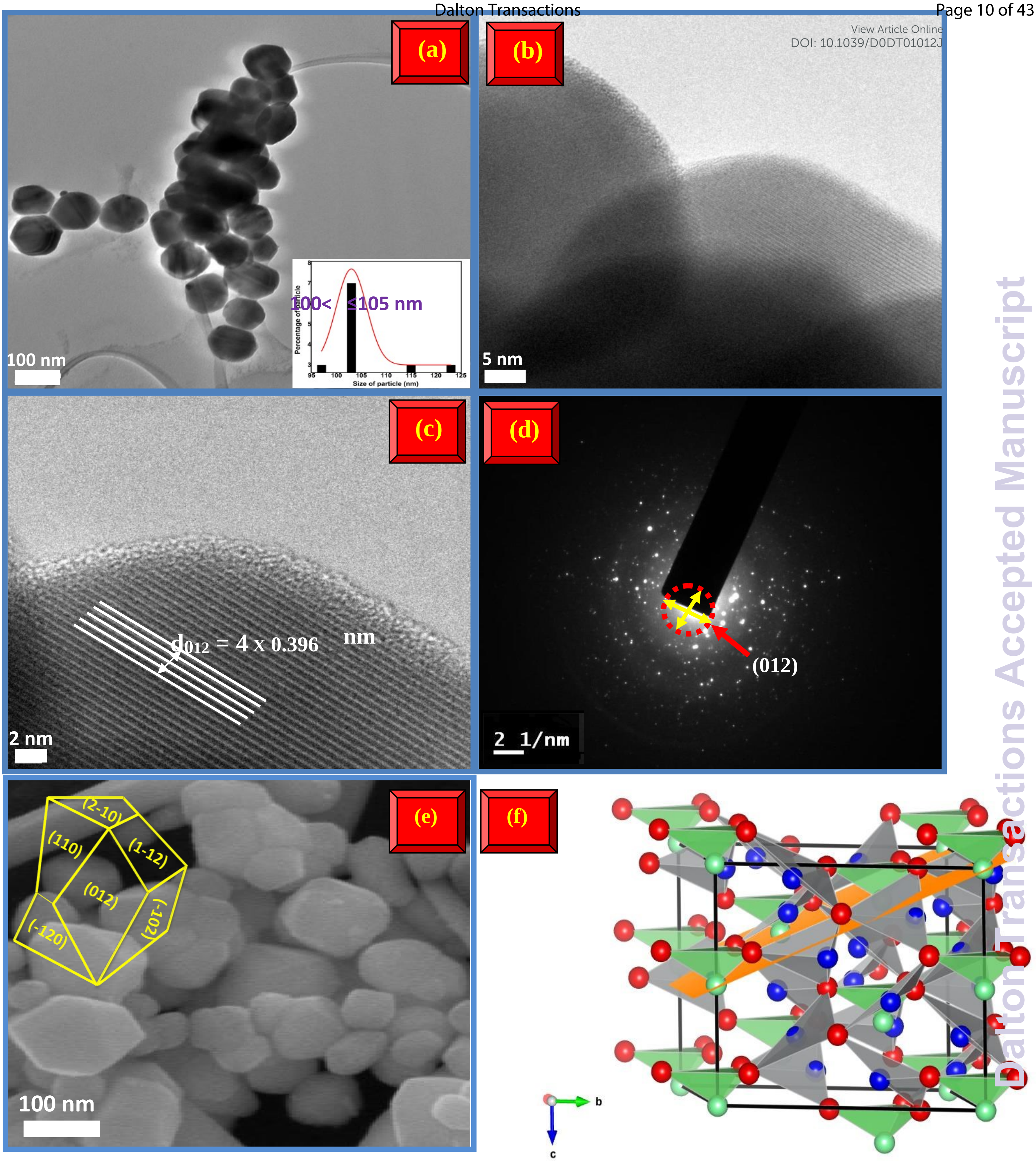

Dalton Transactions Accepted Manuscript

View Article Online
DOI: 10.1039/D0DT01012J

Published on 05 June 2020. Downloaded by University of Exeter on 6/9/2020 8:08:14 PM.

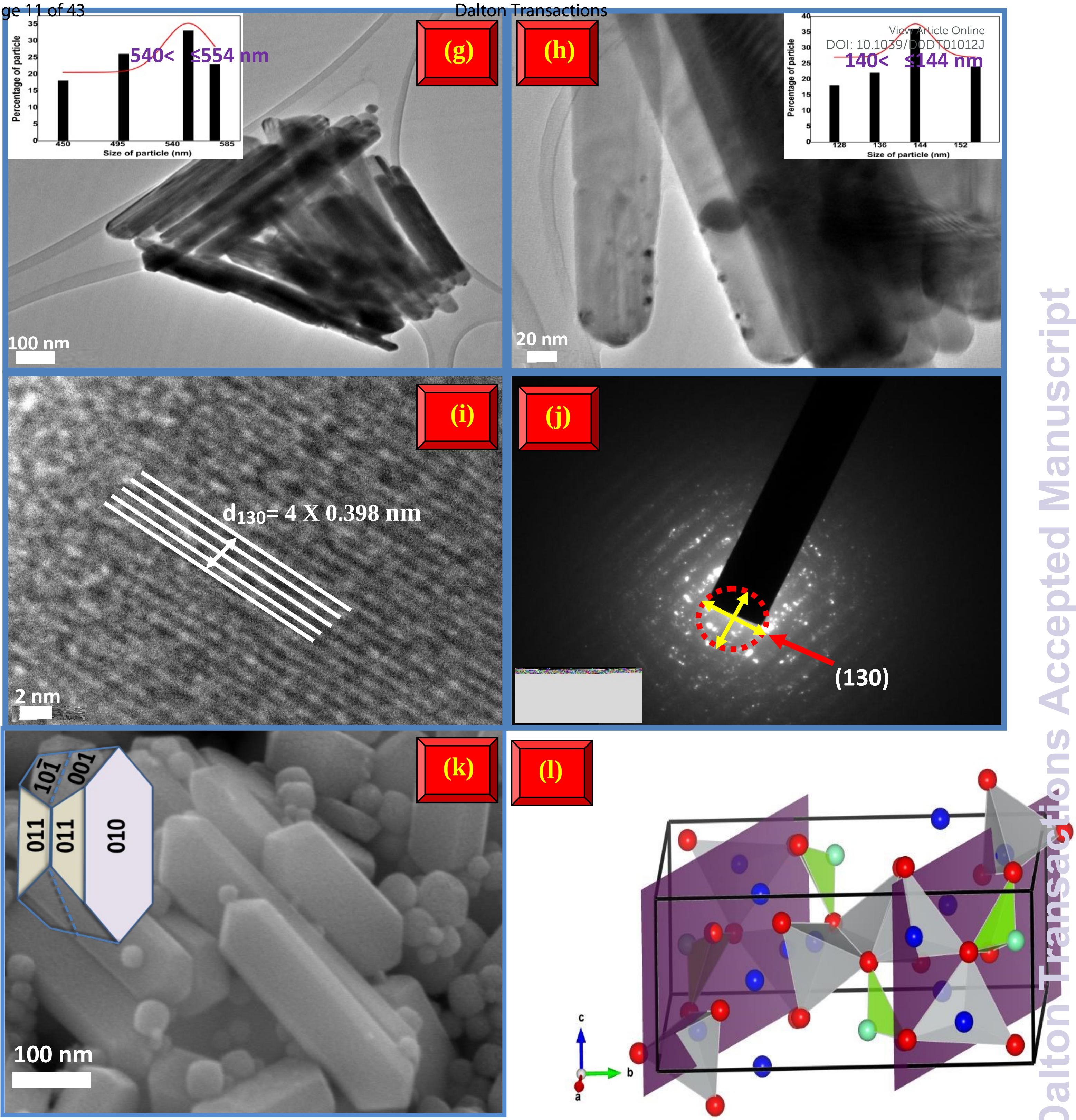

Dalton Transactions Accepted Manuscript

View Article Online
DOI: 10.1039/D0DT01012J

Published on 05 June 2020. Downloaded by University of Exeter on 6/9/2020 8:08:14 PM.

Dalton Transactions Accepted Manuscript

Fig. 3. TEM and SEM image analyses for hexagonal and monoclinic SAS. For hexagonal: (a) TEM image confirms size distribution of quasi spherical particle (inset), (b) High magnification image, (c) Fringe pattern analysis by HRTEM image confirms the inter planar spacing (0.396nm), (d) SAED pattern analysis confirms the characteristic plane (012), (e) SEM image of the corresponding hexagonal prism like particle and its equivalent model assigning possible crystal facets (inset), (f) (012) crystal facet (orange) and possible atomic arrangement in unit cell for the hexagonal system [the atoms are assigned as; Ag(blue), Sb(bottle green) and S(red)]. For monoclinic: (g) TEM image confirms length size distribution of rod shaped particle (inset), (h) High magnification image confirms the breadth size distribution of particle, (i) HRTEM image confirms the inter planar spacing (0.398nm), (j) SAED pattern analysis confirms the characteristic plane (130), (k) SEM image of the corresponding monoclinic ortho-prism particle and its equivalent model assigning possible crystal facets, (l) Possible atomic arrangement and (130) crystal facet (purple) in unit cell for the monoclinic system [the atoms are assigned as; Ag(blue), Sb(bottle green) and S(red)].

In the solvent composition like the mixture of OAm and DDT in a certain ratio (here OAm/DDT =1/1.5)[51] hexagonal SAS was obtained. It has been well studied that DDT was usually used as sulfur (S) source and stabilizer for the growth of metal sulfide nanocrystals.[52] On the other hand OAm shows it's versatility as reducing agent, stabilizer and capping agent.[53] In the hexagonal unit cell, all the three S atoms bonded with Sb gets outward of the wall of the lattice which might be stabilized by the dipole interaction of –SH of DDT and Sb-S bond while OAm worked as a capping agent only. In case of monoclinic system it gets orthoprism (h>k, 0) [here (130)] like structure (Fig. 3k). The (130) facet having all the three Sb-S bonds are aligned with the plane but Ag-S bond is off the plane outward to wall of the lattice. As the dissociation of the $-NH_2$ of

View Article Online
DOI: 10.1039/D0DT01012J

Published on 05 June 2020. Downloaded by University of Exeter on 6/9/2020 8:08:14 PM.

Dalton Transactions Accepted Manuscript

OAm on {010} [crystallographic equivalent of 130 plane] containing Ag-S is faster than DDT so here OAm acted as stabilizer as well as a capping agent for the synthesis of monoclinic NCs.[54] The syntheses of NCs and ligand exchange process are illustrated in Scheme 1.

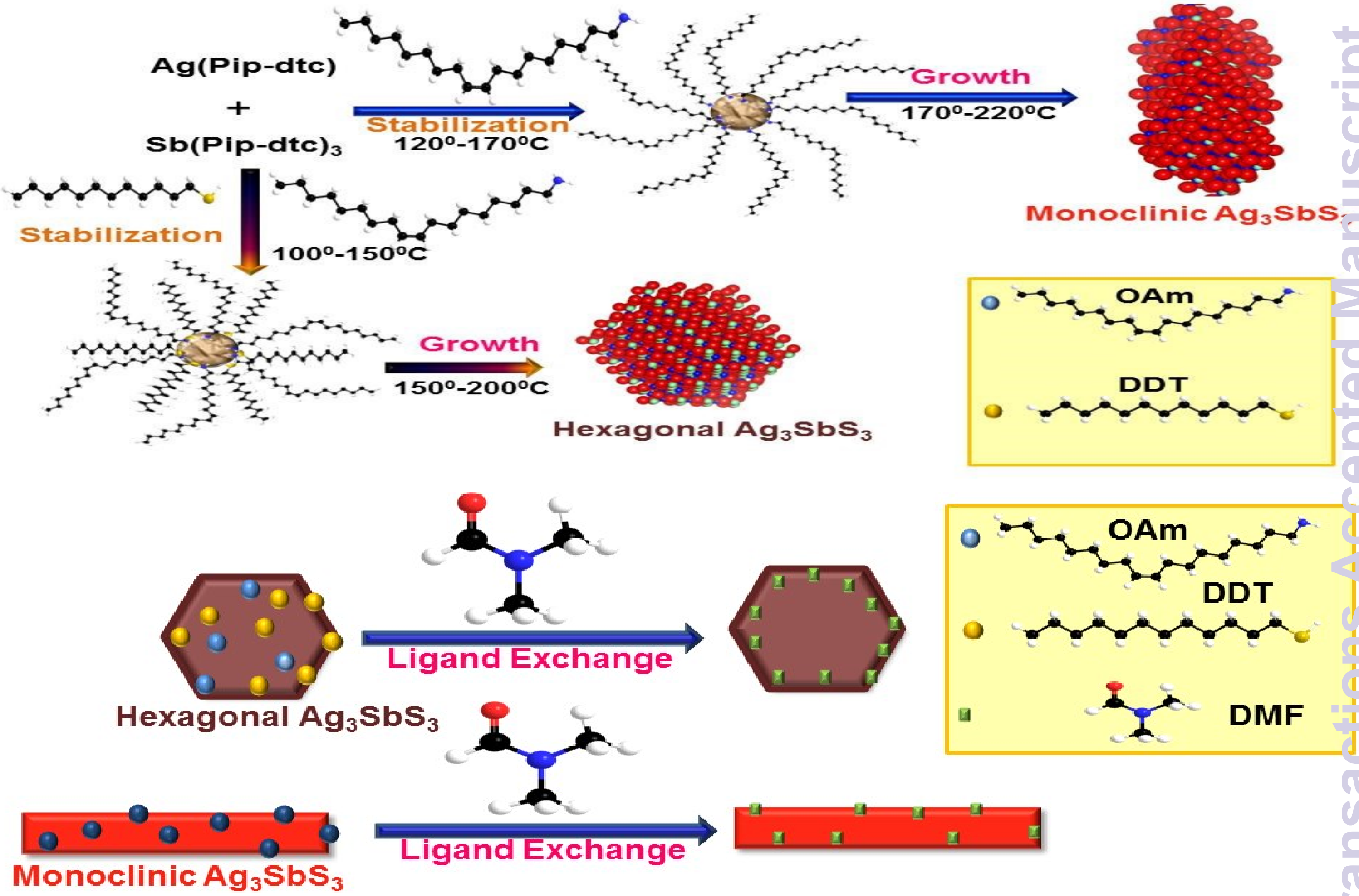

Scheme 1. Schematic manifestation of the preparation of (a) hexagonal SAS and (b) monoclinic SAS NCs and corresponding ligand exchange process.

High-resolution XPS spectra of Ag 3d, Sb 3d, and S 2p for the as-prepared SAS samples are obtained using C 1s as the reference at 284.6 eV (Fig. 4). Binding energy peaks of Ag $3d_{5/2}$ and Ag $3d_{3/2}$ in as-prepared hexagonal SAS sample are at 367.72 eV (Ag 3d5/2) and 373.74 eV (Ag $3d_{3/2}$) (Fig. 4a) and for monoclinic SAS the peaks are at 367.91 eV (Ag 3d5/2) and 373.94 eV

View Article Online
DOI: 10.1039/D0DT01012J

Published on 05 June 2020. Downloaded by University of Exeter on 6/9/2020 8:08:14 PM.

Dalton Transactions Accepted Manuscript

(Ag $3d_{3/2}$) (Fig. 4d). Binding energy peaks of Sb 3d were located at 529.06-530.40 (Sb $3d_{5/2}$) and 538.39-539.65 eV (Sb $3d_{3/2}$) for hexagonal SAS (Fig. 4b) and at 529.17-530.53 eV (Sb $3d_{5/2}$) and 538.53-539.80 eV (Sb $3d_{3/2}$) (Fig. 4e) for monoclinic SAS respectively. For both the cases the binding energies of Sb are slightly higher than that of Sb in Sb_2S_3,[55] indicating a strong bonding of Sb−S in both SAS samples. There are no peaks at 531−532 eV confirms there are no such oxidized SbOx[55] and adsorbed oxygen at the surface of samples which further proves the phase purity of the samples. The high-resolution spectra of S 2p show two peaks for S at 161.24-161.87 eV (for S $2p_{3/2}$) and 163.09 eV (for S $2p_{1/2}$) for hexagonal SAS (Fig. 4c) and at 161.44-162.09 eV (for S $2p_{3/2}$) and 163.20 eV (for S $2p_{1/2}$) (Fig. 4f) that are attributed to a single doublet from S−Sb bonds.[56] The XPS peaks reside between 162.2-163.8 eV are ascribed to metal-sulfur bond having less coordinating divalent sulfide (S^{-2}) ions at the surface. This result is reflected on the binding energy of Sb which is slightly lower in hexagonal than monoclinic SAS and this is due to the stabilization process of off-pane Sb–S in 012 facet by –S of DDT.[57] On the other hand the binding energies of all the elements are higher in monoclinic than hexagonal due to its crystalline saturation as obtained from the crystal structure. Here Ag-S bond might get stabilized through polar interaction by $–NH_2$ of OAm only. Most importantly, all XPS results confirm the presence of following oxidation states: Ag(I), Sb(III) and S(II) which subsequently proves the stoichiometric composition of SAS.

View Article Online

DOI: 10.1039/D0DT01012J

Published on 05 June 2020. Downloaded by University of Exeter on 6/9/2020 8:08:14 PM.

Dalton Transactions Accepted Manuscript

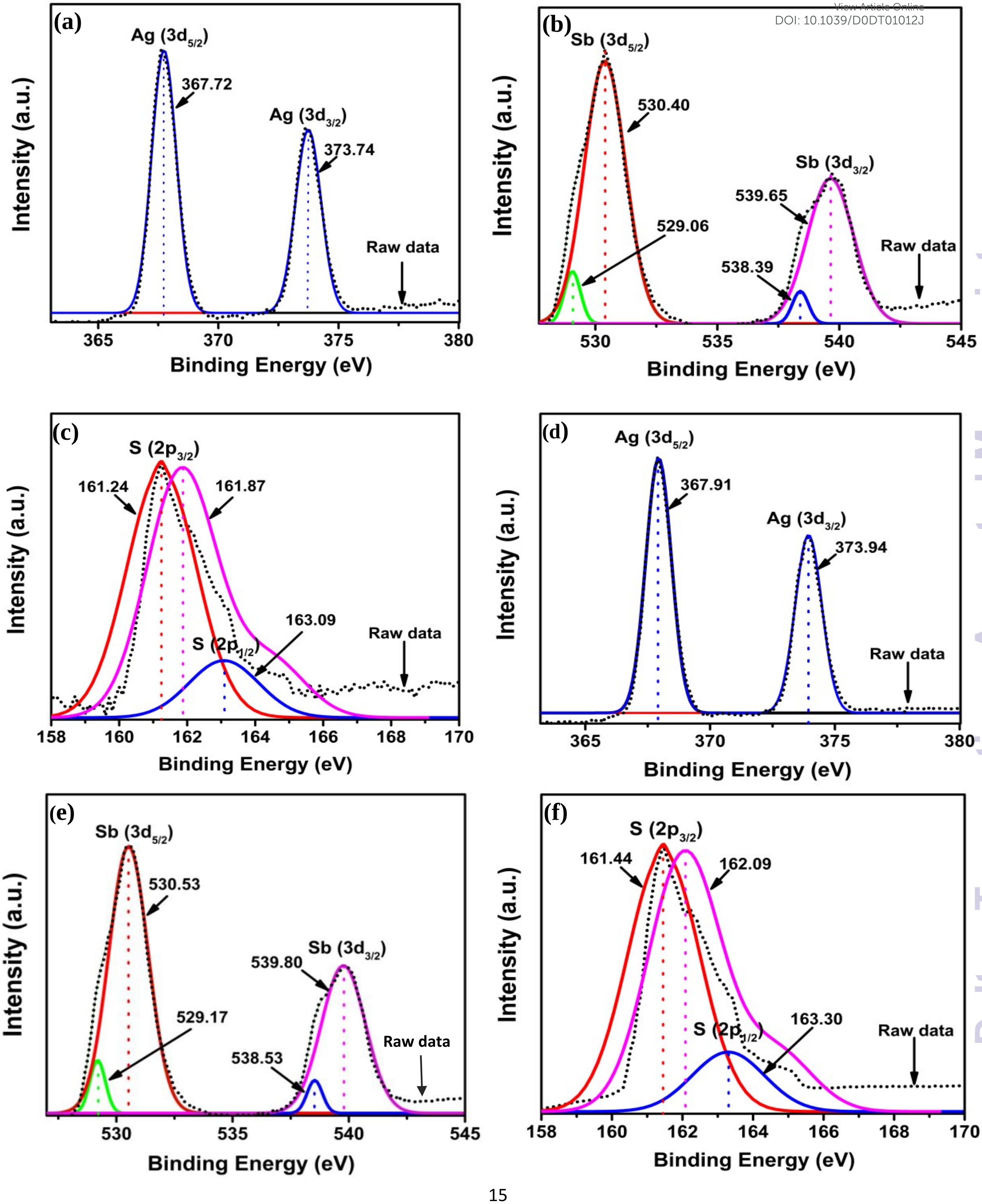

View Article Online
DOI: 10.1039/D0DT01012J

Published on 05 June 2020. Downloaded by University of Exeter on 6/9/2020 8:08:14 PM.

Fig. 4. XPS spectra of hexagonal and monoclinic SAS. Figure (a), (b) and (c) are for hexagonal SAS. (d), (e) and (f) are for monoclinic SAS. Binding energy curves for all data are fitted with Gaussian-Lorentzian function.

To confirm the arrangement of atoms in the crystal, the Raman spectroscopic measurement for both the phases has been done and is shown in Fig. S4 (a) hexagonal and (b) monoclinic. In addition the detailed explanation has also been depicted in supporting information. Also the surface area characterized by nitrogen adsorption/desorption analysis has been demonstrated and explained in supporting information. (Fig. S5 (a) hexagonal and (b) monoclinic). The BET surface area obtained as follows: 230.10 m^2g^{-1} for hexagonal SAS and 252.85 m^2g^{-1} for monoclinic SAS.

On the basis of the excellent physical properties of both materials, at first we have performed a solution based electrocatalytic ORR experiment to explore their response individually and we have obtained that hexagonal SAS does have a notable catalytic activity toward ORR but monoclinic SAS does not (Fig. 5a). Both ORR plots are corresponding to the disk current at 1600 RPM respectively. Importantly, further evaluating the retarding MeOH crossover effect on ORR by adding 3(M) MeOH into O_2 saturated 0.1(M) KOH solution, we have distinctly observed that hexagonal SAS has significant ORR selectivity and MeOH tolerance much higher than commercial Pt/C but here the observation of responses of monoclinic SAS (Fig. 5b) toward MeOH surprises us most and leads us to make use of this material in MOR. These interesting results have driven us to explore the phase dependent catalytic activities for two different energy applications.

Dalton Transactions Accepted Manuscript

View Article Online
DOI: 10.1039/D0DT01012J

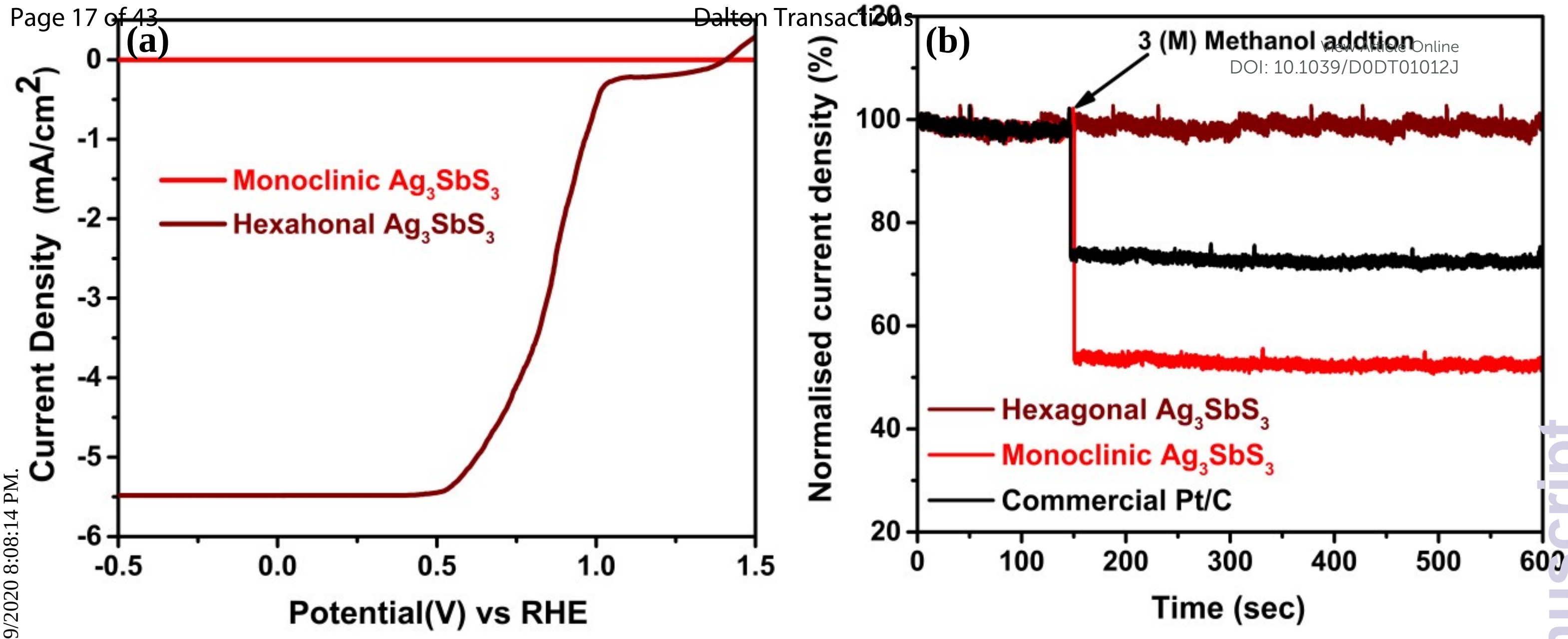

Fig. 5. (a) Comparative ORR activity study for both hexagonal and monoclinic SAS. (b) Chronoamperometric measurements in O_2 saturated 0.1(M) KOH for different catalyst before and after addition of 3(M) MeOH.

Then we have evaluated the electronic properties of both SAS semiconductor NCs which depend upon the band edge position and band gap. Here conduction band edge is associated with the Ag 5s orbital whereas the valence band edge is produced by Sb 5p and S 3p orbital.[55] The valence band energy maxima is associated with electrons having vector k=0. The transitions between valence band maxima to conduction band minima are indirect in nature whereas the band edges reside in other places of Brillouin zone.[58] To obtain the semiconducting properties, probable band position and band gap we have performed electrochemical Mott-schottky analyses[59-61] combining with electronic spectra of both the materials. Electronic spectra are shown in Fig. S6. (a) hexagonal and (b) monoclinic SAS. Their band gap has been obtained to be 1.65 eV for hexagonal and 2.1 eV for monoclinic SAS. The absorption edge for monoclinic resides around 600 nm so deep red colour of monoclinic SAS was observed but in case of hexagonal some blue shift occurs due to decrease in Sb content (obtained from EDX analysis) and so the colour has been obtained as deep brown. This kind of phase dependent band intensity variation occurs due

Published on 05 June 2020. Downloaded by University of Exeter on 6/9/2020 8:08:14 PM.

Dalton Transactions Accepted Manuscript

View Article Online
DOI: 10.1039/D0DT01012J

Published on 05 June 2020. Downloaded by University of Exeter on 6/9/2020 8:08:14 PM.

Dalton Transactions Accepted Manuscript

to electronic delocalization and covalent character.[60] The large orbital of Sb leads to less orbital overlapping with S and also the electronegativity difference between Sb and S define the less covalent and more ionic property of SAS NCs than any other mixed-valence ternary transition metal sulfide NCs. The typical Mott-schottky analyses are shown in Fig. S7 ((a) hexagonal, (b) monoclinic and (c) comparative demonstration of band energy diagram). The negative slope of the plot (a) indicates that the hexagonal SAS has p type and the positive slope of the plot (b) confirms monoclinic SAS has n type semiconducting property. The flat band potentials (E_{FB}) are as follows: 2.65 V for p type hexagonal SAS which corresponds to valence band whereas -1.02 V Vs. RHE for n type monoclinic SAS which refers to conduction band by convention. It is to be noted that in case of light induced MOR low band gap of monoclinic SAS favors PEC reaction than TiO_2 having large band gap. On the other hand, though hexagonal SAS has lower band gap than monoclinic SAS but it does not help in MOR because the charge carrier helps in oxidation is hole which belongs to valence band and the valence band maxima for hexagonal SAS resides at 2.65V, that is far away from the onset potential of MOR which starts from 0.23V vs RHE. The same argument might be implanted for the non-participation of monoclinic SAS for ORR. Here the responsible charge carrier is electron in the conduction band and the conduction band minima for monoclinic SAS is at -1.02V which is quite distant from the potential of ORR (1.23V) and hence monoclinic SAS does not favor ORR. Moreover photoluminescence (PL) lifetime study (Fig. 6) reveals that the probability of electron hole pair recombination is very much less in case of monoclinic than hexagonal SAS after visible light excitation. Lifetime parameter investigation (in picosecond) on incorporating bi-functional decay relation: $F(t)= A_1 \exp(-t/\tau_1) + A_2 \exp(-t/\tau_2) + A_0$ shows that the band edge decay (τ_2) has been influenced higher than the decay in deep

View Article Online
DOI: 10.1039/D0DT01012J

trap states (τ_1)[62,63]. The value of τ_2 for hexagonal and monoclinic SAS are 7.95 and 2356.04 ps whereas the value of τ_1 for the same are 1.25 and 53.21 ps.

Published on [illegible] June 2020. Downloaded by University of E[illegible] on [illegible] PM.

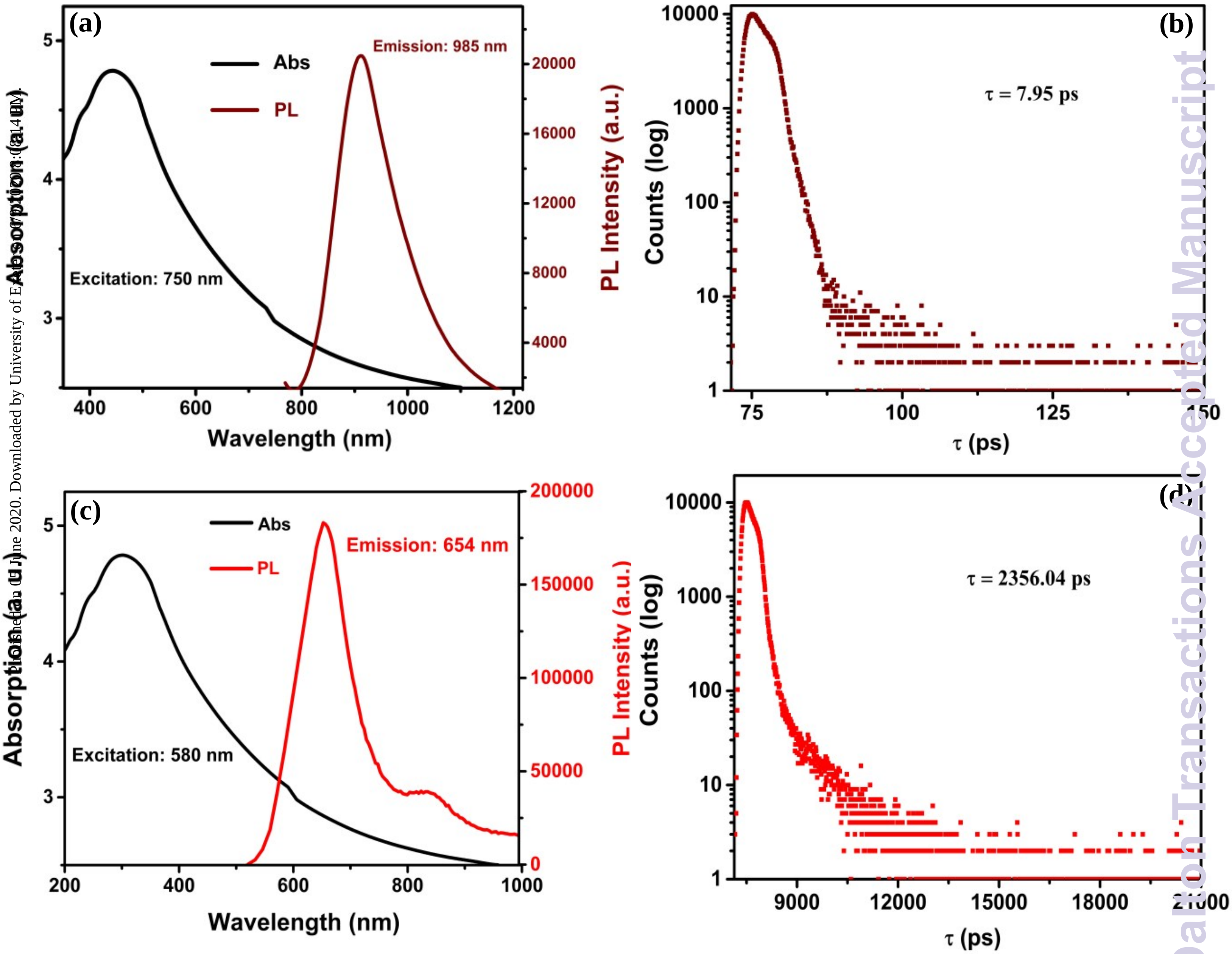

Dalton Transactions Accepted Manuscript

Fig. 6. Electronic and corresponding PL spectra for (a) Hexagonal and (c) Monoclinic**.** Life time measurements for the same (b) and (d).

View Article Online
DOI: 10.1039/D0DT01012J

Published on 05 June 2020. Downloaded by University of Exeter on 6/9/2020 8:08:14 PM.

Dalton Transactions Accepted Manuscript

Fourier Transform Infra-Red (FTIR) spectra of individual organic ligands along with the NCs before and after exchange of ligands are shown in Fig. S8.

Nyquist plots and the corresponding Bode plots have been obtained from Electrochemical Impedence Spectroscopy (EIS) measurements which are shown in Fig. S9 and S10. Fig. S9 (a) represents comparative impedance study for ORR between commercial Pt/C and hexagonal SAS, (b) shows corresponding Bode plot. The same sequence is maintained at for MOR also (Fig. S10). Here the absence of higher frequency semicircle and the presence of only lower frequency semicircle confirm, both ORR and MOR are kinetically controlled process but not the mass transfer process.[64] The data are tabulated in Table S1. The values of solution resistance (R_S) are near about equal as all the EIS were obtained in 0.1 (M) KOH and the small R_S value indicate less ohmic loss in electrolyte. The hexagonal SAS exhibits slightly lower charge transfer resistance (R_{ct}) than Pt/C which means faster charge transfer happens on semiconducting surface than on the metallic surface for ORR.[65] Similar result is reflected for MOR between monoclinic SAS and TiO_2, but here the difference in R_{ct} is much higher than ORR. Also the higher frequency for both the SAS NCs in Bode plots indicate the lifetime of electrons is shorter i.e. faster charge transfer kinetic has been taken place than in case of Pt/C and TiO_2.[66]

Before get into the whole electrochemical procedure for ORR and MOR in KOH medium, we have tested and purified the commercial KOH. The procedure of testing of trace elements in KOH and the purification process has been depicted in supporting information. The amount of trace element obtained by Inductively Coupled Plasma Mass Spectroscopy (ICPMS) has been tabulated in Table S2. The ORR polarization curves in commercial and pure KOH have been shown in Fig. S11.

View Article Online
DOI: 10.1039/D0DT01012J

Published on 05 June 2020. Downloaded by University of Exeter on 6/9/2020 8:08:14 PM.

At first we have performed a cyclic voltammetry (CV) for ORR within the potential range 0-1.25 V Vs. RHE under saturated N_2 and then O_2 atmosphere in 0.1(M) KOH (Fig. S12). It has been shown that hexagonal SAS is very much prone to response to ORR. The comparative study between hexagonal SAS and commercial Pt/C is shown in Fig. 7(a) and the corresponding bar diagram for onset potential (E_{onset}) and half wave potential ($E_{1/2}$) are shown in Fig. 7(b). The values of E_{onset} and $E_{1/2}$ for SAS are 1.09 and 0.86 V whereas for Pt/C, 0.88 and 0.73 V Vs. RHE respectively and this superiority of our material encouraged us to perform ORR. LSV curves in Fig. 7(c) illustrate the limiting rotating ring disc electrode (RRDE) speed (1625 RPM) for maximum current density and also the first order kinetics has been obtained from the corresponding linear Koutecky-Levich (K-L) plots[67,68] (inset in Fig. 7c) for 0.4, 0.5, 0.6 and 0.7 V Vs. RHE. Solving the K-L equation, number of electron (n) transfer has been calculated as follows: 3.85, 3.88, 3.90 and 3.94 for SAS (Fig. 7d) and 3.90, 3.90, 3.93 and 3.95 for Pt/C at the corresponding potentials (Fig. S13). The kinetics of the ORR has been defined by Tafel slopes[69-71] (Fig. 7e) which indicates that the ease of adsorption and activation of O_2 on SAS over Pt/C.[67] The result was obtained to be 50.30 and 58.52 mV dec^{-1} for hexagonal SAS and commercial Pt/C respectively. Moreover ECSA normalized specific activity and mass activity at 0.75 V Vs. RHE for both hexagonal SAS and commercial Pt/C are compared (Fig. 7f) and again the hexagonal SAS is far superior than Pt/C. Data are tabulated in Table S3.

Dalton Transactions Accepted Manuscript

View Article Online
DOI: 10.1039/D0DT01012J

Published on 05 June 2020. Downloaded by University of Exeter on 6/9/2020 8:08:14 PM.

Dalton Transactions Accepted Manuscript

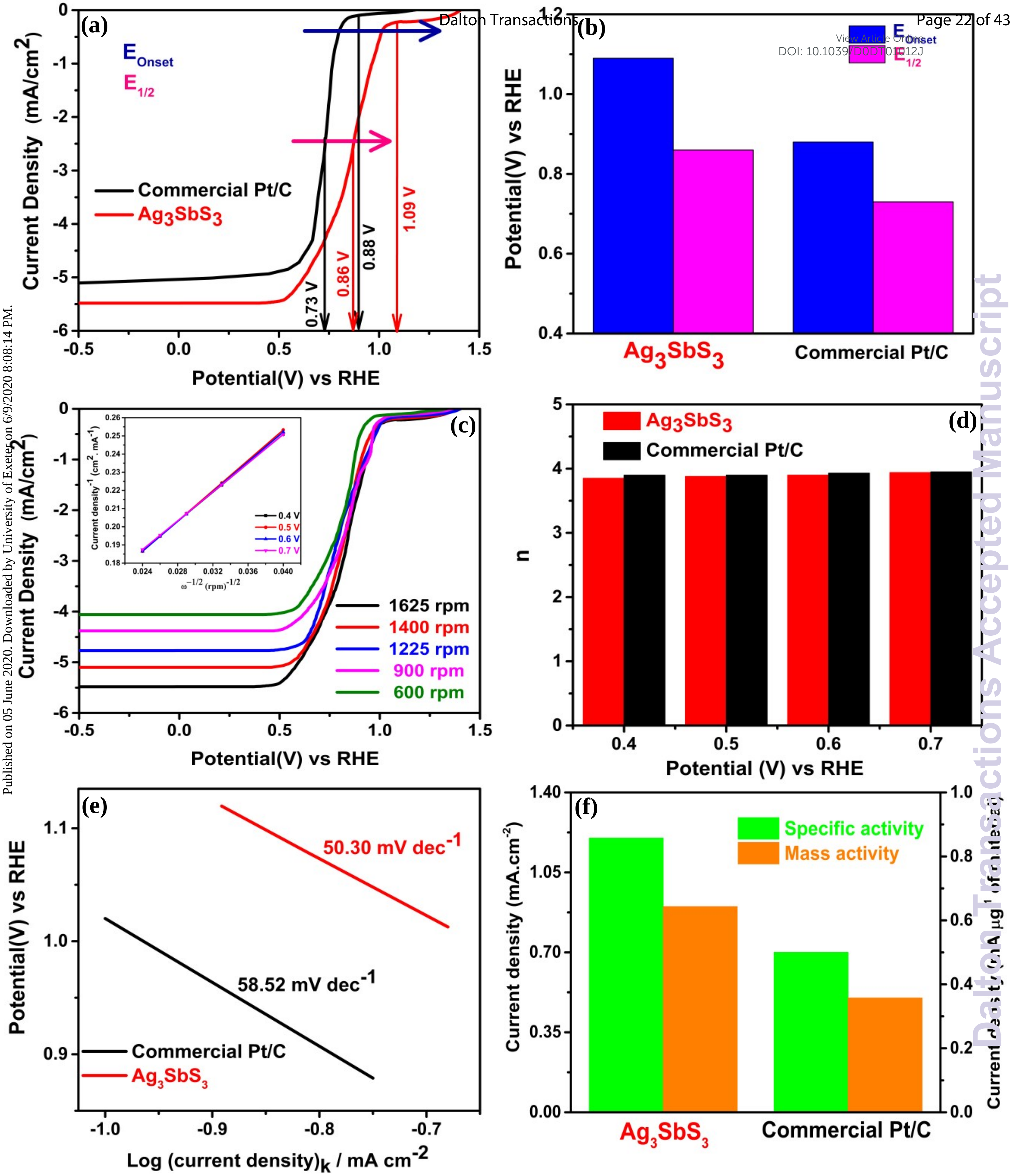

View Article Online
DOI: 10.1039/D0DT01012J

Published on 05 June 2020. Downloaded by University of Exeter on 6/9/2020 8:08:14 PM.

Dalton Transactions Accepted Manuscript

Fig. 7. (a) ORR polarization curve for commercial Pt/C and hexagonal SAS. (b) Onset potential and half wave potential bar diagram for materials. (c) ORR polarization curve for different rotational speed and K-L plot (inset). (d) The number of electron transferred bar diagram within potential range 0.3-0.8 V Vs. RHE. (e) Tafel slopes for materials. (f) Specific and mass activity bar diagram for materials.

Comparing between ring current and disk current along with percentage of H_2O_2 yield Vs. n are shown in Fig. 8(a) and (b). It is shown that the H_2O_2 (%) is lower for hexagonal SAS (12.1 %) than Pt/C (14.6 %) as the number of electron transferred approaches to near four. It has been confirmed that ORR leads to higher extent of water formation in case of our material than Pt/C. In order to investigate the long term stability and reproducibility; chronoamperometric measurement and CV with 5000 cycles have been allowed to run. Fig. 8(c) shows that the relative current density reaches to 69% for SAS whereas it is 55% for commercial Pt/C after the whole course of chronoamperometric study for 50 hours. Fig. 8(d) shows reproducible nature of ORR activity by our material and that has been persistent from 1st cycle to 5000th cycle. Further to evaluate stability and reusability, we have characterized our materials by XRD and TEM analyses after electrochemical experiments (Fig. S1a and S3a) indicating there are no substantial changes of phase as well as morphology which eventually support the stability and reusability for the concerned application. Durability test was also performed for Pt/C (Fig. S14) which also supports superior durability of our material. Further we have evaluated electrochemical active surface area (ECSA) from double layer charge capacitance (C_{dl}) by performing CV in O_2 saturated 1(M) KOH at different scan rates ranging from (20-100 mV/sec) for both hexagonal SAS and commercial Pt/C[72] (Fig. S15). The capacitive currents were measured at 1.2 V Vs. RHE and the corresponding linear plots are shown in Fig. 8(e). We can see that C_{dl} gets increased by

View Article Online
DOI: 10.1039/D0DT01012J

hexagonal SAS compared to Pt/C which reflects in the value of ECSA. Interestingly we have found a linear correlation between BET, C_{dl}, and ECSA (Table S4) as expected and has been demonstrated by the bar diagram shown in Fig. 8(f). Loss of normalized ECSA(%) for both hexagonal SAS and Pt/C have been shown in Fig. S16. Comparative literature study for complete electrochemical ORR by various ternary metal sulfides NC is illustrated in Table S5.

Published on 05 June 2020. Downloaded by University of Exeter on 6/9/2020 8:08:14 PM.

Dalton Transactions Accepted Manuscript

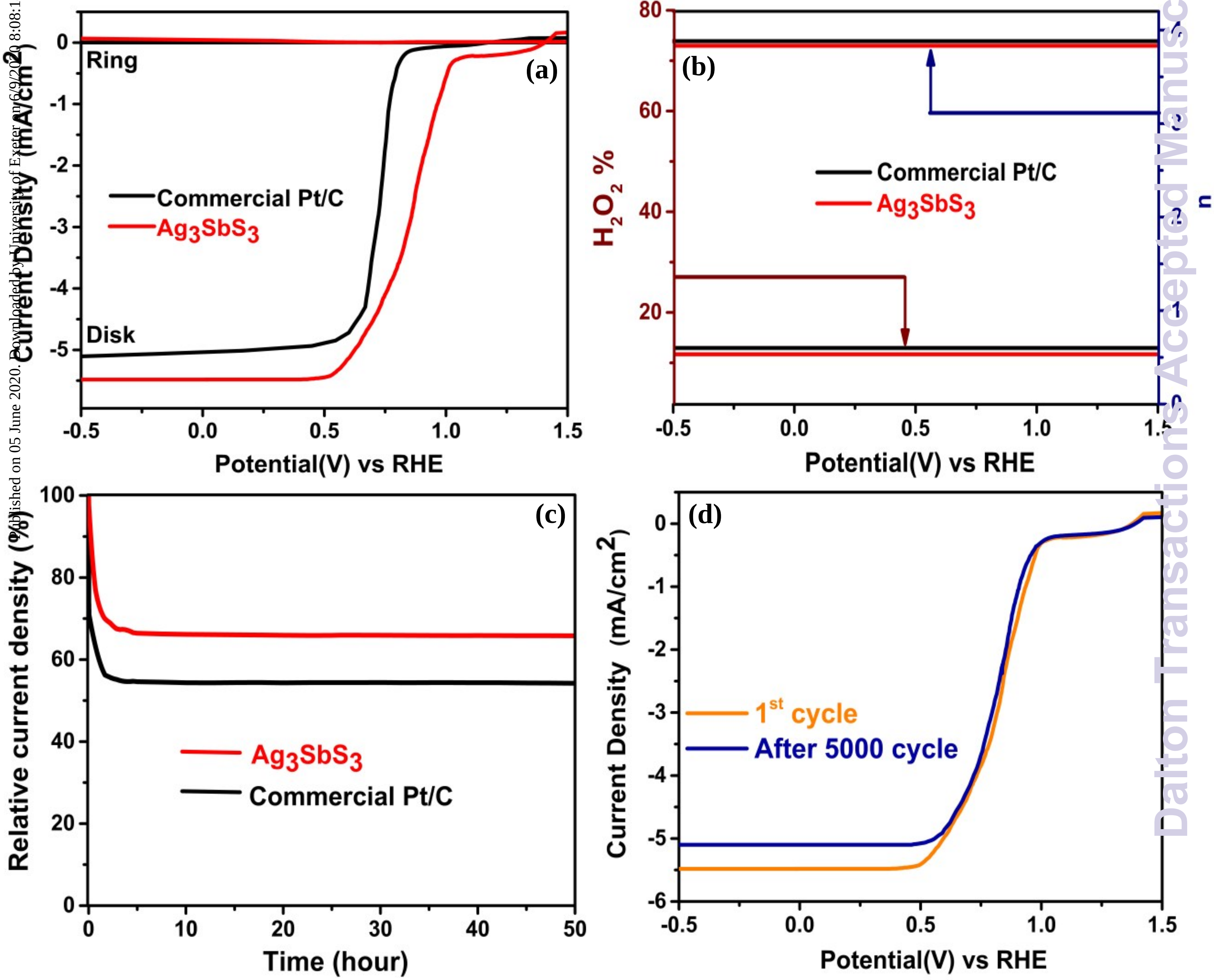

View Article Online
DOI: 10.1039/D0DT01012J

Published on 05 June 2020. Downloaded by University of Exeter on 6/9/2020 8:08:14 PM.

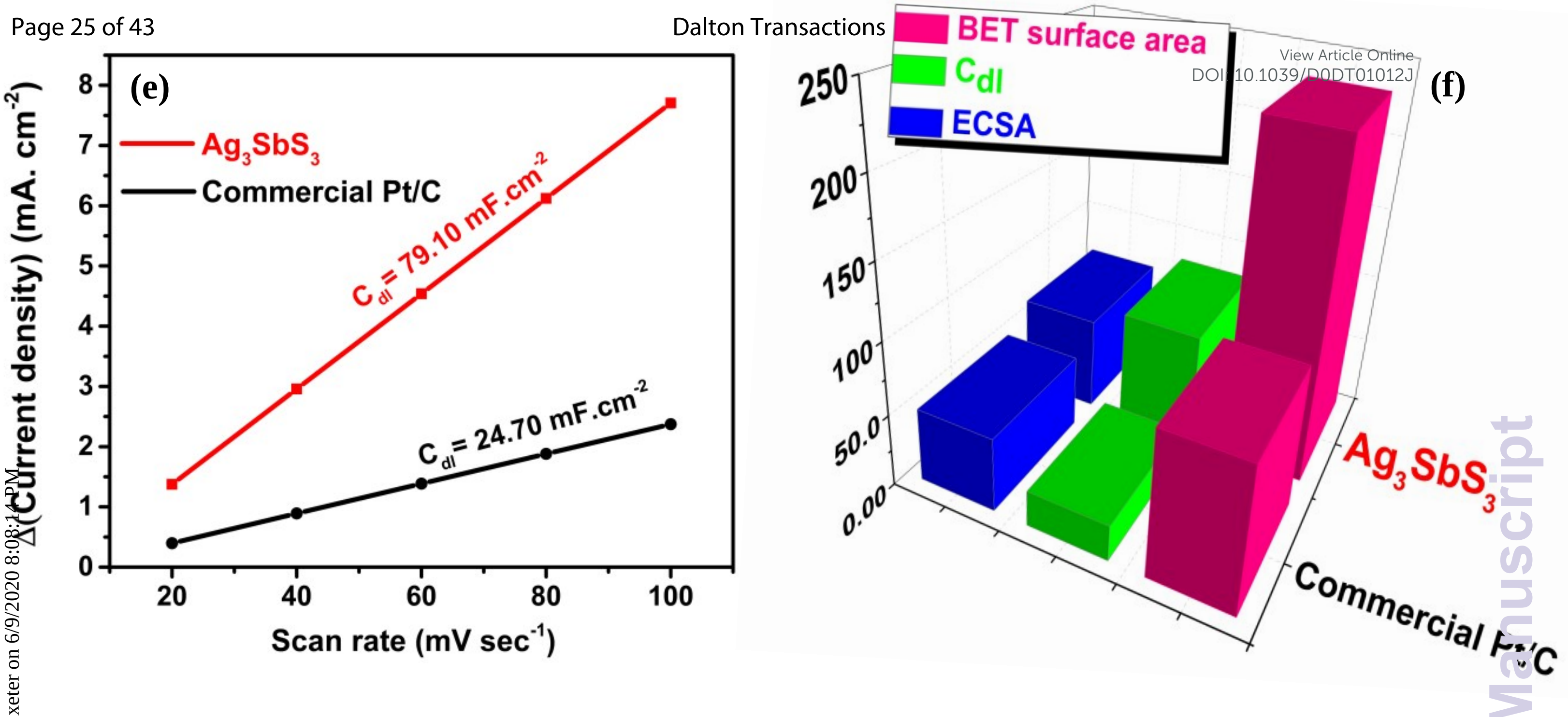

Fig. 8. (a) Ring current and disk current density obtained from RRDE test. (b) H_2O_2 % and number of electron transferred for hexagonal SAS and Pt/C. (c) Comparative chronoamperometric stability measurement for fifty hours. (d) Durability test by LSV curves for 1st and after 5000th cycle for ORR on hexagonal SAS. (e) The capacitive currents are measured under different scan rates (20, 40, 60, 80, 100 mV.sec^{-1}). (f) Comparative bar diagram for BET surface area, C_{dl} and ECSA for corresponding material.

To have a clear theoretical insight about the ORR activity of hexagonal SAS we have performed density functional theory (DFT) calculation for the overall reaction pathways on the catalytically active site (Fig. 9). The whole computational methods are described in supporting information. From the HRTEM and SAED pattern analysis; (012) plane has been constructed for the SAS slab. The computational hydrogen electrode (CHE) method has been employed to predict the overall electrode process i.e. potential limiting step and theoretical limiting potential. Here from the energy profile diagram the limiting step might be OOH* formation (1st step) and the associated free energy (ΔG) have been obtained to be -1.0 eV. The limiting electrode potential

Dalton Transactions Accepted Manuscript

View Article Online
DOI: 10.1039/D0DT01012J

Published on 05 June 2020. Downloaded by University of Exeter on 6/9/2020 8:08:14 PM.

that keeps all the elementary reaction steps exothermic is called working potential (U) of fabricated electrode by the corresponding catalyst.[24] Here above 1.0 V the limiting step gets endothermic and this is close consistent with the experimental onset potential (1.09 V) which is higher than the theoretical working potential (0.73 V) for Pt/Cu(100). Moreover the calculated binding energy for O_2 on the catalytic surface has been obtained as -0.85 eV that is quite close to that of -1.10 eV on Pt catalyst[73]. Further the reduction of OOH^* to O^* and not to OOH^- has been proven by the thermodynamical investigation as OOH^* to OOH^- is endothermic by 0.22 eV whereas OOH^* to O^* is exothermic by -0.25 eV. The possible adsorption sites for intermediate species (OOH^*, O^* and OH^*) are shown in Fig. 9(a), (b) and (c) after optimization. The corresponding relative free energy diagram for different intermediate species at U= 0, U= 1.0 and U=1.23 V have been shown in Fig. 9 (d), (e), (f) and (g).

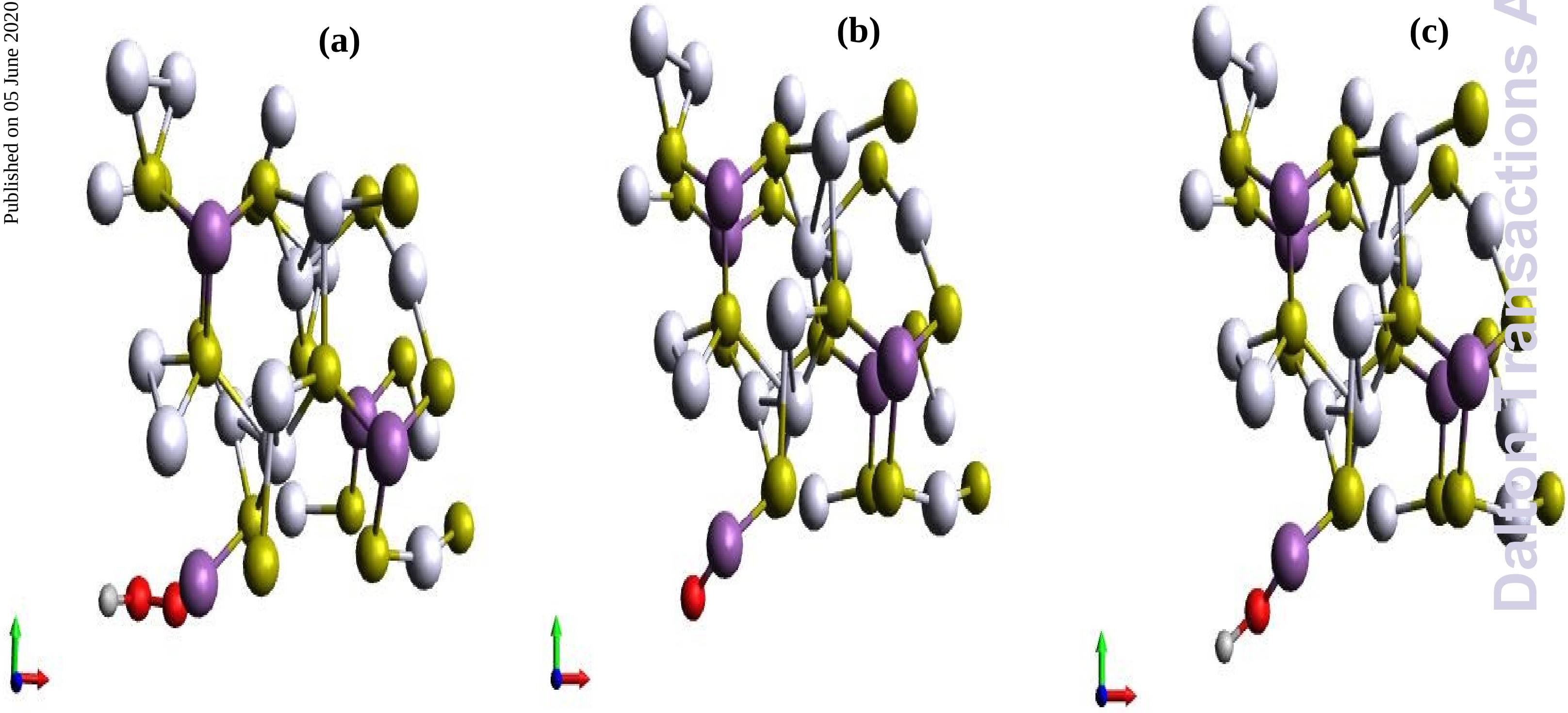

Dalton Transactions Accepted Manuscript

View Article Online
DOI: 10.1039/D0DT01012J

Published on 05 June 2020. Downloaded by University of Exeter on 6/9/2020 8:08:14 PM.

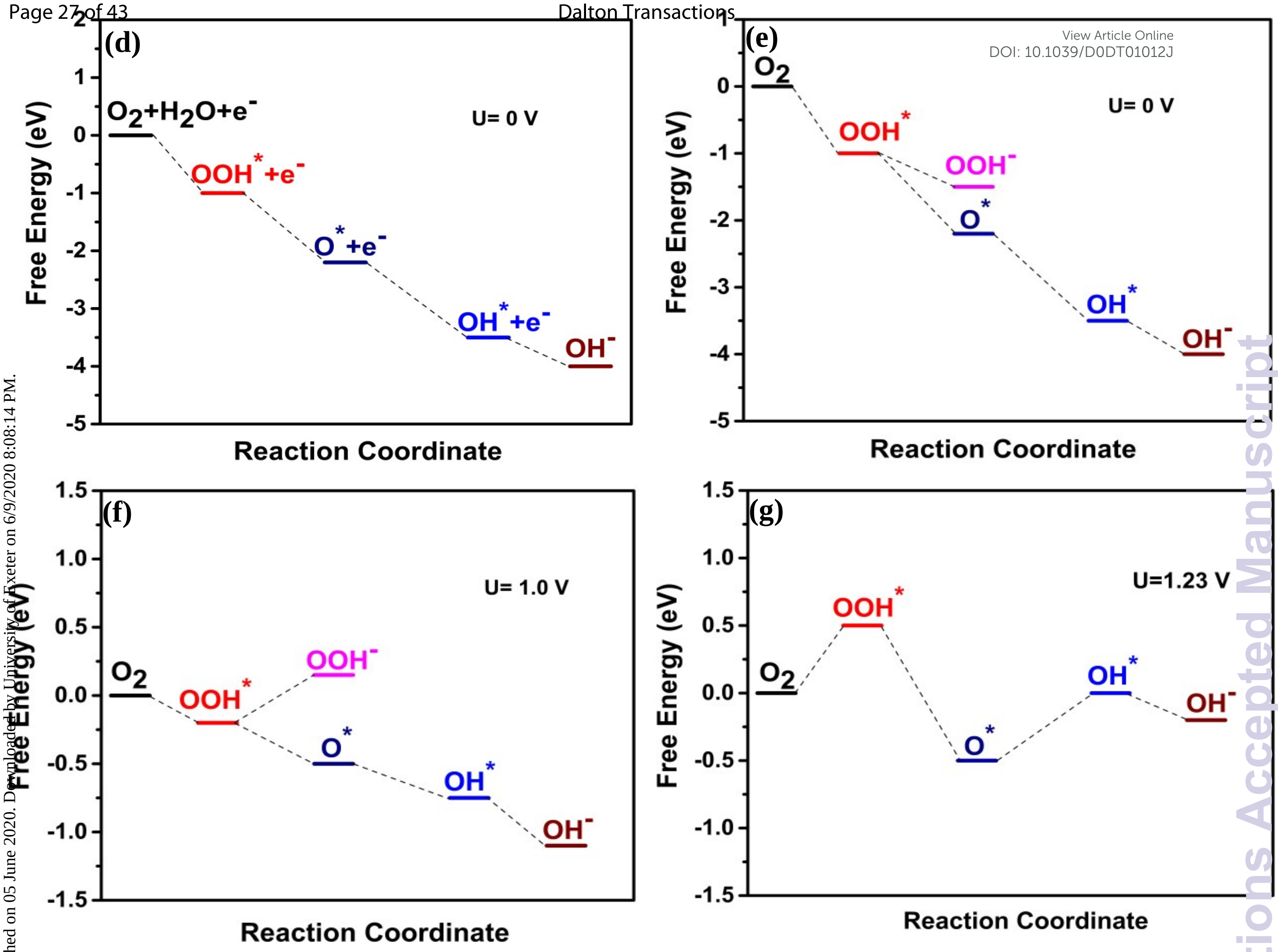

Fig. 9. Side view for the adsorption of the intermediate species (a) OOH^*, (b) O^*, (c) OH^* on the 012 plane of hexagonal SAS. Comparison of the free energy (ΔG) diagram of ORR on hexagonal SAS (012) plane at U=0 (d, e), U=1.0 (f) U=1.23 V (g).

TiO_2 has widely been used photocatalysts due to its non-toxicity, low cost, moderate efficiency and stability. TiO_2-P25 consists of anatase (75%) and rutile (25%) phases which are both photoactive and due to lower conduction band edge of rutile than anatase, electron might get transferred from anatase to rutile to reduce the electron hole pair recombination possibility. But the main problem for TiO_2 is its large bad gap which restricts TiO_2 for being used as a

Dalton Transactions Accepted Manuscript

View Article Online
DOI: 10.1039/D0DT01012J

Published on 05 June 2020. Downloaded by University of Exeter on 6/9/2020 8:08:14 PM.

Dalton Transactions Accepted Manuscript

photocatlyst under visible light.[74] On the other hand to suppress the surface poisoning, neutral CO removal is required which is formed during MOR along with other unwanted oxygenated species. The energy required for desorption of neutral CO by dissociative fashion is about 2.2-3.0 eV which corresponds to visible to near UV light[75]. In our case, forward current (I_f) to backward current (I_b) ratio (I_f/I_b) is obtained to be 8.30 which is satisfactorily high for removing CO and other oxygenated species. Moreover the monoclinic SAS semiconductor NC exhibits exceptional photosensitivity and stability in MeOH under visible light illumination and this is mainly due to its convenient band gap as well as its high charge carrier. From the slope of the Mott-schottky plot, using the equation; **Slope = $2/e\varepsilon\varepsilon_0 N$, [where, ε (dielectric constant of NC) = 17.17, ε_0 (permittivity of vacuum) = 8.854 X 10^{-12} $m^{-3}.kg^{-1}.S^4.A^2$, e (electronic charge) = 1.6 X 10^{-19} C, N = charge carrier]** the charge carrier has been obtained as **1.23 X 10^{17}** and this is quite high value of charge carrier that could accelerate a PEC reaction efficiently. We have addressed the entire possible important determining factors by doing comparative study of electro-oxidation of MeOH under visible light irradiation on the surface of monoclinic SAS and TiO_2 separately. At first we have measured CV in the Ar saturated mixture of electrolyte containing 0.1 (M) KOH and 0.1 (M) MeOH to make sure about the oxidative response of our material. Fig. 10(a) shows two distinct peaks at around 0.6 V which might correspond to MeOH adsorption on the surface and the higher peak starts at 0.9 V continues to 1.1 V due to oxidation of MeOH. After evaluation of oxidative response we have compared our material with most extensively used semiconductor TiO_2 by performing CV under dark (Fig. 10b). We can see our material produces ~10 times higher current density than TiO_2 (1.8/0.18) under dark. Thereafter we have evaluated the whole MOR further under illumination. Compared to dark, current density increases about 25 times under illumination of visible light which is shown in Fig. 10(c). Then

View Article Online
DOI: 10.1039/D0DT01012J

Published on 05 June 2020. Downloaded by University of Exeter on 6/9/2020 8:08:14 PM.

Dalton Transactions Accepted Manuscript

from I-V curve (Fig. 10d) under chopped light illumination for MOR, nearly 20 times higher photocurrent density was obtained in case of our material than mesoporous TiO_2. Upon illumination of visible light onto the electrode surface, charge separation occurs between valence band (VB) and conduction band (CB). The hole generated in VB is responsible for PEC oxidation of methanol whereas electron resides on CB moves through the circuit and produces photocurrent. From the onset potential, increase in PEC potential eases the charge separation which continuously facilitates the overall redox reaction and finally whole procedure resulted in substantial increase of photocurrent density. Enhancement of relative photocurrent density under light irradiation **$[(I_{Light}-I_{Dark}/I_{Dark}) \times 100]$** has been the key determining factor which has been obtained to be 845 at onset potential (0.73 V Vs. RHE) for SAS which are much higher than any other TiO_2 based catalyst used in MOR so far. Moreover the position of valence band maxima of a semiconductor which is responsible for electrochemical oxidation of any organic substance, resides at 1.08 V (Vs. RHE) for SAS whereas it resides at 3.0 V (Vs. RHE) for TiO_2 (at pH 13) and the conventional onset potential for MOR starts at 0.23 V Vs. RHE (Fig. S7c). The most probable product of whole oxidation process might be formaldehyde because the FTIR spectroscopic titration (liquid) has been done throughout one hour at a definite time interval which is shown in Fig. S17. The corresponding peak identification has been illustrated in supporting information. This confirms the oxidation reaction might get ceased with the formation of aldehyde within this potential window. The characteristic peak for hydroxyl group of methanol (-OH) gets lowered with time as expected. The relative study in terms of stability and durability (Fig. 10e) between our material and TiO_2 by chronoamperometric measurements[76,77] (at 0.5 V Vs. RHE) reveals that relative photocurrent density becomes 52% for SAS and 7% for TiO_2 after 50 hour experiment which confirms that our material can carry the stable energy

View Article Online
DOI: 10.1039/D0DT01012J

Published on 05 June 2020. Downloaded by University of Exeter on 6/9/2020 8:08:14 PM.

Dalton Transactions Accepted Manuscript

output to a higher extent for an extended period of time than TiO_2. Here also we have performed XRD and TEM analyses to investigate stability and reusability of our material after the whole PEC experiments and shown in Fig. S1(b) and S3(b). There are no such significant changes in the characteristics peaks (XRD) in Fig. S1(b) and the material could retain its morphology (TEM) as well (Fig. S3b); which support that our material is highly stable as well as reusable for this application. Moreover we have run a sensitivity optimization study (Fig. 10f) by carrying out CV experiment on successive addition of MeOH by micropipette into 15 ml 0.1 (M) KOH from a 1(M) MeOH stock solution (from 300-3000 µL for 20-200 mM) and the sensitivity toward MeOH was found to be around 0.1 mA. $cm^{-2}.mM^{-1}$. We have seen that around 20 fold increment of photocurrent has been taken place for this concentration range. Then we have obtained a linear relation (Fig. 10g) between the peak photocurrent density and concentration, based upon the following equation: **$\log(I) = \log(k) + n \log(C)$**, Where I is the peak photocurrent density, k is rate constant, n is the reaction order and C is the bulk concentration of methanol. The high k value (83.17) and increasing peak current indicate less activation energy and diffusion control pathway of the corresponding MOR under illumination.[75] With higher methanol concentration, diffusion into the interface of the NCs might accelerate the reaction. This is also confirmed by the CV experiment in 0.1 (M) KOH and 0.1(M) MeOH under illumination in different scan rates (5-100 mV/sec) (Fig. 10h). Here the peak current density linearly depends upon the square root of the scan rate which is a characteristic phenomenon of a diffusion control pathway.[78]

View Article Online
DOI: 10.1039/D0DT01012J

Published on 05 June 2020. Downloaded by University of Exeter on 6/9/2020 8:08:14 PM.

Dalton Transactions Accepted Manuscript

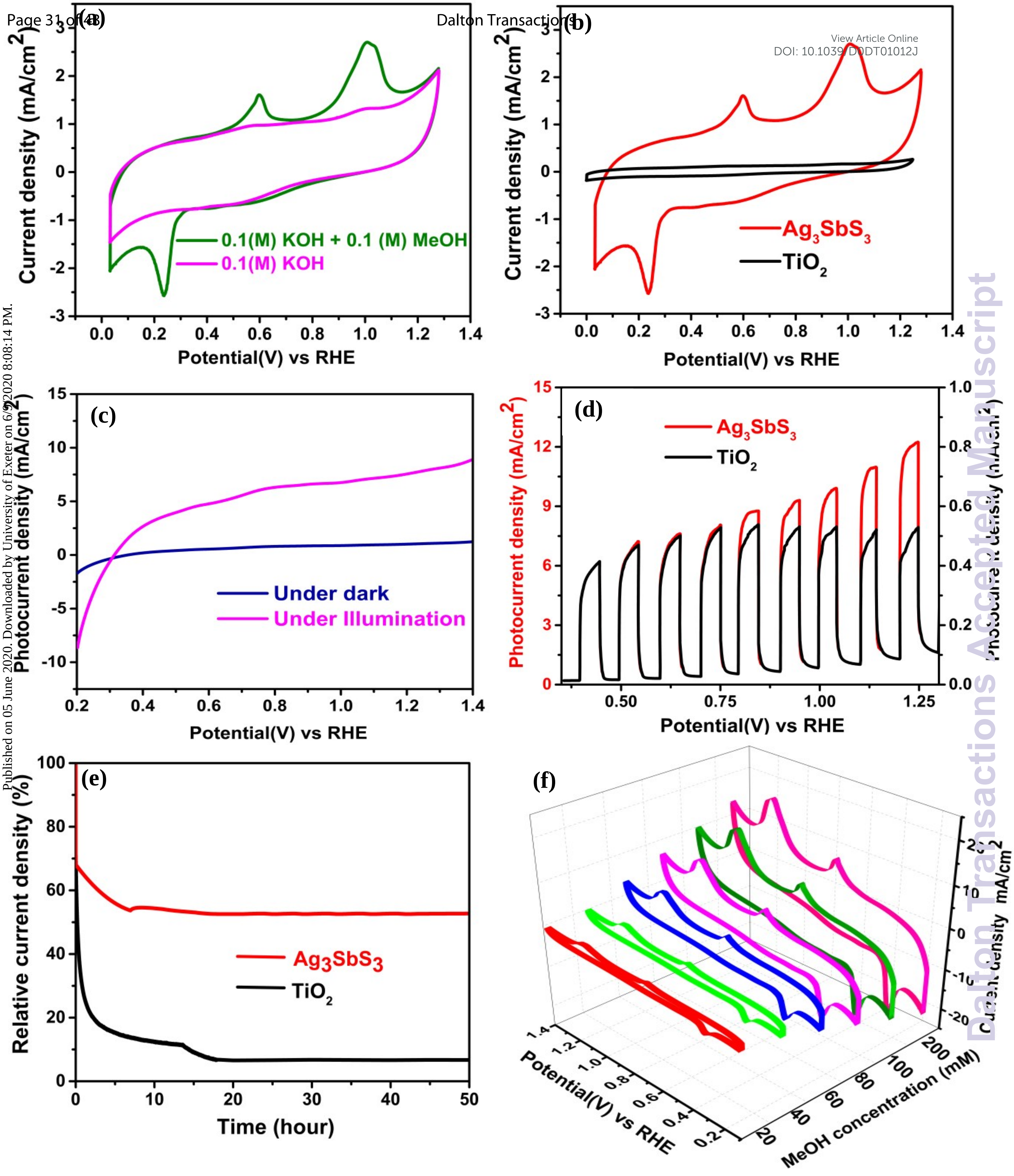

View Article Online
DOI: 10.1039/D0DT01012J

Published on 05 June 2020. Downloaded by University of Exeter on 6/9/2020 8:08:14 PM.

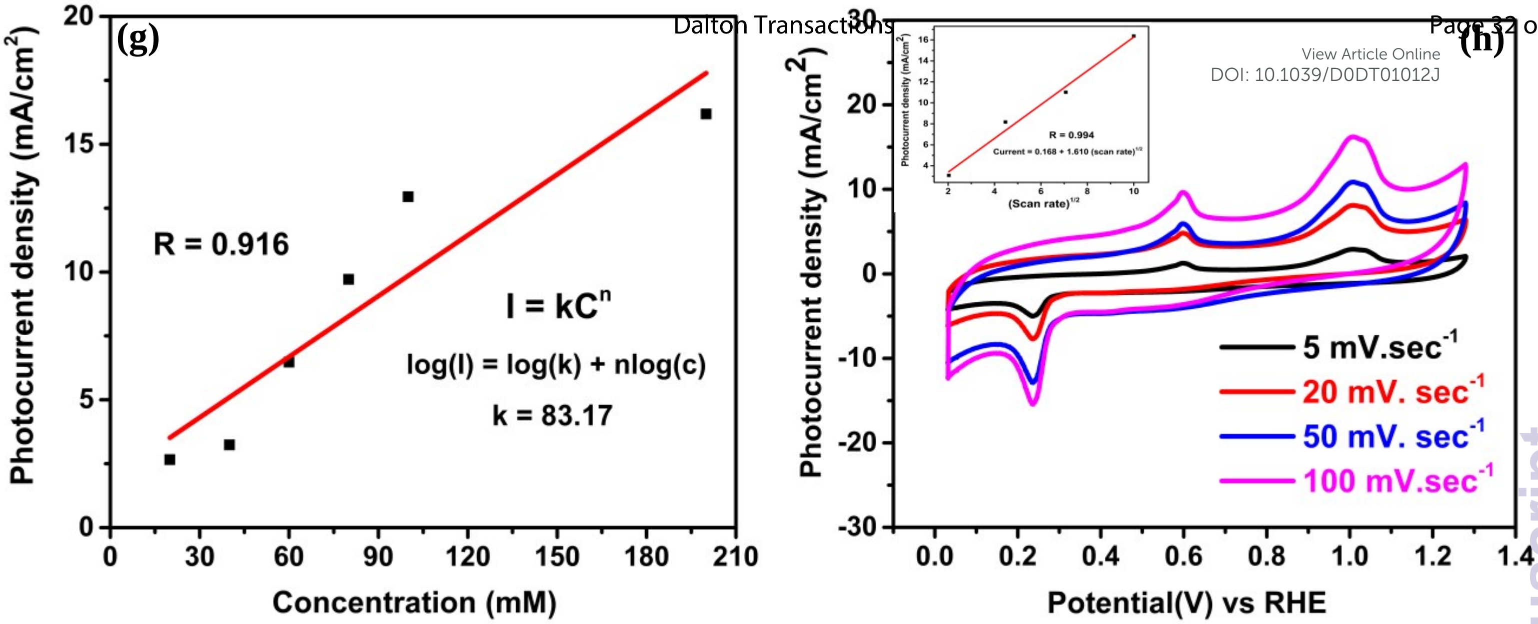

Fig. 10. (a) MOR activity test by CV in 0.1 (M) KOH and then in the mixture of 0.1 (M) KOH and 0.1 (M) MeOH. (b) Comparative CV measurement between our material and TiO_2 under dark. (c) LSV response in dark Vs. light of the fabricated photoanode by our material in presence of MeOH. (d) Sensitivity test by LSV under chopped illumination for both the materials. (e) Photocurrent stability measurement by chronoamperometry for fifty hours. (f) MeOH sensing test for the MeOH on the fabricated photoanode under illumination (concentration ranging from 20-200 mM). (g) Photocurrent density Vs. concentration plot to evaluate rate constant. (h) Photocurrent density variation with different scan rate.

The photoanode fabricated by hexagonal SAS also exhibits outstanding stability during CV run at different electrocatalytic cycles (Fig. S18). It has been observed that after 1200 cycles the onset potential was almost unchanged and MOR activity possess above 85%. The photo induced MeOH oxidation was extensively studied on various metal based TiO_2 catalyst and we have undergone a comparative study which is demonstrated in Table S6.

The ORR and MOR catalytic activities by phase pure two SAS NCs are mainly due to their mixed valence, band structure, high surface area and large calatalytic active sites. Firstly, mixed

Dalton Transactions Accepted Manuscript

View Article Online
DOI: 10.1039/D0DT01012J

Published on 05 June 2020. Downloaded by University of Exeter on 6/9/2020 8:08:14 PM.

Dalton Transactions Accepted Manuscript

valence may provide certain donor-acceptor chemisorption site for reversible adsorption of O_2 and OH^- in case of ORR at low over potential. Secondly, desirable band structure and charge carrier density for monoclinic SAS may be responsible for the higher photo-induced electrocatalytic activity toward MOR in solution. Third, the high surface area and mesoporous nature of both NCs might be served to reduce charge transfer resistance, to facilitate the reflex space for rapid ion transmission and overall to provide large active sites for related electrochemical reactions.

Conclusion

In summary, we have developed a new synthetic strategy to design bifunctional SAS, hexagonal for ORR and monoclinic for photo induced MOR. The hexagonal SAS comes out to be a stable and cheaper catalyst than commercial Pt/C which shows higher ORR activity than Pt/C and some recently developed ternary metal sulfide catalysts in terms of mass and specific activity, onset and half wave potential. On the other hand, photoanode fabricated by monoclinic SAS also exhibits higher photo induced MOR activity than widely used TiO_2 and noble metal based TiO_2 catalysts in terms of enhancement of photocurrent density, sensitivity and stability as it accumulates sufficient photogenerated hole on the catalytic surface. The large specific BET surface area as well as ECSA has done a crucial role for this kind of electrochemical performances. Most importantly, these two phases show pronounced electrocatalytic activities due to their excellent physiochemical properties. So, we may conclude that our study might explore a new way of designing semiconductor electrocatalyst by simply changing solvent polarity with implications for phase dependent electrochemical applications.

View Article Online

DOI: 10.1039/D0DT01012J

Published on 05 June 2020. Downloaded by University of Exeter on 6/9/2020 8:08:14 PM.

Dalton Transactions Accepted Manuscript

Supporting Information

Physical Measurement, Device Fabrication for Photoelectrochemical Methanol Oxidation Reaction (PEC-MOR) and Oxygen Reduction Reaction (ORR), Electrochemical Characterization of Fabricated Device, Computational Method Details, Powder XRD patterns and TEM analyses of materials after electrolysis, SEM-EDX, Elemental Composition, Elemental Mapping, Raman Spectroscopy, BET Analysis, UV-Vis Spectroscopy, Mott-Schottky Analysis and Probable Band Diagram, FTIR spectral analysis of solvent ligands, Nyquist Plots, Bode Plots, Table for Resistance Parameters; CV, LSV, K-L plot, Durability by LSV for ORR; Stability test by CV for MOR; Table containing ICPMS data for commercial KOH, ORR polarization plot in commercial and purified KOH solution, Table of specific and mass activity data for ORR, Capacitance Measurement by CV for ORR; Table for surface area parameters, Plot for loss of normalized ECSA, FTIR spectra for the electrolyte of MOR at different time interval, comparison tables for electrochemical ORR and photo induced MOR.

Conflict of interest

There is no conflict of interest to declare.

Acknowledgement

Authors are grateful to Dr. Divesh N. Srivastava, Principal Scientist, Analytical Division, Central Salt and Marine Chemicals Research Institute, Bhavnagar, India, for providing us instrumental and analytical facilities. The authors are indebted to UGC-RGNF India (ID: RGNF-2015-17-SC-WES-690) and MHRD India for financial assistance. The authors are also thankful to the Department of Chemistry, IIEST, Shibpur, for providing instrumental facilities.

View Article Online
DOI: 10.1039/D0DT01012J

Published on 05 June 2020. Downloaded by University of Exeter on 6/9/2020 8:08:14 PM.

Dalton Transactions Accepted Manuscript

References

1. M. K. Debe, *Nature.*, 2012, **6,** 43-51.
2. J. Li, S. Ghoshal, W. Liang, M. T. Sougrati, F. Jaouen, B. Halevi, S. McKinney, G. McCool, C. Ma, X. Yuan, Z. F. Ma, S. Mukerjee and Q. Jia, *Energy Environ. Sci.*,2016, **9**, 2418-2432.
3. C. W. B. Bezerra, L. Zhang, K. Lee, H. Liu, A. L. B. Marques, E. P. Marques, H. Wang and J. Zhang, *Electrochim. Acta.*, 2008, **53**, 4937–4951.
4. T. Zhou, Y. Du, S. Yin, X. Tian, H. Yang, X. Wang, B. Liu, H. Zheng, S. Qiao and R. Xu, *Energy Environ. Sci.*, 2016, **9**, 2563–2570.
5. J. H. Myung, D. Neagu, D. N. Miller and J. T. S. Irvine, *Nature.*, 2016, **537**, 528–531.
6. H. W. Liang, X. Zhuang, S. Brüller, X. Feng and K. Müllen, *Nat. Commun.*, 2014, **5**, 1–7.
7. K. Strickland, E. Miner, Q. Jia, U. Tylus, N. Ramaswamy, W. Liang, M. T. Sougrati, F. Jaouen and S. Mukerjee, *Nat. Commun.*, 2015, **6**, 1–8.
8. J. A. Varnell, E. C. M. Tse, C. E. Schulz, T. T. Fister, R. T. Haasch, J. Timoshenko, A. I. Frenkel and A. A. Gewirth, *Nat. Commun.*, 2016, **7**, 1–9.
9. S. R. Pendlebury, E. Pastor, Y. Ma, F. Le Formal, M. T. Mayer, M. Gra and J. R. Durrant, *J. Am. Chem. Soc.*, 2017, **139**, 11537-11543.
10. I. L. Granone, K. Nikitin, A. Emiline, R. Dillert, D. W. Bahnemann, *Chemistry Select.*, 2019, **4,** 1232-1239.

View Article Online
DOI: 10.1039/D0DT01012J

Published on 05 June 2020. Downloaded by University of Exeter on 6/9/2020 8:08:14 PM.

11. S. Mohajernia, S. Hejazi, P. Andryskova, G. Zoppellaro, O. Tomanec, R. Zboril, P. Schmuki, *ChemElectroChem.*,(Accepted article), https://doi.org/10.1002/celc.201900076.

12. B. Klahr, S. Gimenez, O. Zandi, F. F.Santiago, T. Hamann, *ACS Appl. Mater. Interfaces.*, 2015, **7**, 14, 7653-7660

13. L. Bu, S. Guo, X. Zhang, X. Shen, D. Su, G. Lu, X. Zhu, J. Yao, J. Guo and X. Huang, *Nat. Commun.*, 2016, **7**, 1–10.

14. M. Escudero-Escribano, P. Malacrida, H. M. Hansen, U. Vej-Hansen, A. Velazquez-Palenzuela, V. Tripkovic, J. Schiøtz, J. Rossmeisl, I. E. L. Stephens and I. Chorkendorff, *Science (80)*, 2016, **352**, 73–76.

15. Q. Li, X. Wen, G. Wu, H. T. Chung, R. Gao and P. Zelenay, *Angew. Chem.*, 2015, **14260**, 7634–7638.

16. Y. Nie, L. Li and Z. Wei, *Chem. Soc. Rev.*, 2015, **44**, 2168–2201.

17. V. Georgakilas, J. N. Tiwari, K. C. Kemp, J. A. Perman, A. B. Bourlinos, K. S. Kim and R. Zboril., *Chem. Rev.*, 2016, **116**, 5464-5519.

18. Z. Zhang, X. Wang, G. Cui, A. Zhang and X. Zhou, *Nanoscale.*, 2014, **6**, 3540–3544.

19. J. Wu, S. Dou, A. Shen, X. Wang, Z. Ma and C. Ouyang, *J. Mater.Chem. A.*, 2014, **2**, 20990–20995.

20. X. Feng, Q. Jiao, H. Cui, M. Yin, Q. Li, Y. Zhao, H. Li, W. Zhou and C. Feng, *ACS Appl. Mater. Interfaces*, 2018, **10**, 29521–29531.

Dalton Transactions Accepted Manuscript

View Article Online
DOI: 10.1039/D0DT01012J

21. W. Liu, J. Zhang, Z. Bai, G. Jiang, M. Li, K. Feng and L. Yang, *Adv. Funct. Mater.*, 2018, **1706675**, 1–11.

22. J. Jiang, S. Lu, H. Gao, X. Zhang and H. Yu, *Nano Energy*, 2016, **27**, 526–534.

23. S. Zhao, Y. Wang, Q. Zhang, Y. Li, L. Gu, Z. Dai, S. Liu, Y. Lan, M. Han and J. Bao, *Inorg. Chem. Front.*, 2016, **3**, 1501-1509.

24. G. Fu, J. Wang, Y. Chen, Y. Liu, Y. Tang, J. B. Goodenough and J. Lee, *Adv. Energy. Mater.*, 2018, **1802263**, 1–12.

25. J. Guo, Y. Shi, X. Bai, X. Wang and T. Ma, *J. Mater. Chem. A.*, 2015, **3**, 24397–24404.

26. S. Ganguli, S. Das, S. Kumari, H. R. Inta, A. K. Tiwari and V, Mahalingam, *ACS Omega.*, 2018, **3**, 9066-9074.

27. H. R. Inta, T. Biswas, S, Ghosh, R. Kumar, S. K. Jana and V, Mahalingam, *ChemNanoMat.*,(Just Accepted), https://doi.org/10.1002/cnma.202000005.

28. J. Theerthagiri, R.A. Senthil, B. Senthilkumar, A. R. Polu, J. Madhavan and M. Ashokkumar, *J. Solid State Chem.*, 2017, **252**, 43–71.

29. T. Huang, H. Fang, L. Xu, Z. Wang, Y. Xin, J. Yu and S. Yao, *J. Catal.*, 2018, **359**, 223–232.

30. X. Rui, H. Tan and Q. Yan, *Nanoscale.*, 2014, **6**, 9889–9924.

31. C-H. Huang and O. Knop, Can. *J. Chem.*, 2011, **49**, 598-602.

Published on 05 June 2020. Downloaded by University of Exeter on 6/9/2020 8:08:14 PM.

Dalton Transactions Accepted Manuscript

View Article Online
DOI: 10.1039/D0DT01012J

Published on 05 June 2020. Downloaded by University of Exeter on 6/9/2020 8:08:14 PM.

Dalton Transactions Accepted Manuscript

32. J. Yang, X. Shen, J. Wei, L. Zhang, D. Zhao and B. Yao, *Catal. Sci. Technol*., 2016, **6**, 7604–7614.

33. G.J.T. Brink, I.W.C.E. Arends, R. A. Sheldon, *Science*., 2000, **287**, 1636–1639.

34. C. Wang, F. Jiang, R. Zhou, Y. Du, P. Yang, C. Wang and J. Xu, *Mater. Res. Bull*., 2013, **48**, 1099–1104.

35. G. Palmisano, E. García-López, G. Marcì, V. Loddo, S. Yurdakal, V. Augugliaro and L. Palmisano, *Chem. Commun*., 2010, **46**, 7074–7089.

36. C. Maheu, E. Puzenat, C. Geantet, L. Cardenus, P. Afanasiev, *Int. J. Hydrogen Energy*., 2019, **44**, 18038-18049.

37. J. D. Feichtner, R. Johannes and G. W. Roland, *Appl. Opt*., 1970, **9**, 1716-1717.

38. Y. A. M. Olikh, *Phys. stat. sol*., 1983, **81**, 1–5.

39. K. A. Schönau and S. A. T. Redfern, *J. Appl. Phys*., 2002, **92**, 7415–7424.

40. T. Daniel, J. Henry, K. Mohanraj and G. Sivakumar, *Mater. Res. Express*, 2016, **3**, 1–10.

41. T. Daniel, J. Henry, K. Mohanraj and G. Sivakumar, *Mater. Chem. Phys*., 2016, **181**, 415–421.

42. C. L. Chou, N. Suriyawong, B. Aragaw, J. Bin Shi and M. W. Lee, *J. Electrochem. Soc*., 2016, **163**, H445–H449.

43. M. Gussain, P. Rawat and R. Nagarjan, *Mat. Res. Bulletin*., 2014, **60**, 872–875.

44. Y. Xu, L. Yuan, R. Xie, L. Wang, Q. Liang, Z. Geng, H. Liu and K. Huang, *Cryst. Growth*

View Article Online
DOI: 10.1039/D0DT01012J

Published on 05 June 2020. Downloaded by University of Exeter on 6/9/2020 8:08:14 PM.

Dalton Transactions Accepted Manuscript

Des., 2018, **18**, 864–871.

45. D. Xu, S. Shen, Y. Zhang, H. Gu and Q. Wang, *Inorg. Chem*., 2013, **52**, 12958–12962.

46. P. R. Brown, D. Kim, R. R. Lunt, N. Zhao, M. G. Bawendi, J. C. Grossman and V. Bulovi, *ACS Nano*., 2014, **8**, 5863–5872.

47. G. Gabka, P. Bujak, M. Gryszel, K. Kotwica and A. Pron, *J. Phys. Chem. C.* 2015, **119**, 9656-9664.

48. R.S. Selinsky, J.H. Han, E.A. Morales Pérez, I.A. Guzei and S. Jin, *J. Am. Chem. Soc*., 2010, **132**, 15997-16005.

49. C. Di, J. Ngoune, C. Pettinari, B. W. Skelton and A. H. White, *Inorg. Chim. Acta*., 2007, **360**, 2935–2943.

50. W. N. Kun, P. O. Brien, P. D. Mcnaughter, L. D. Nyamen, B. F. Spencer, P. T. Ndifon and N. Revaprasadu, *RSC. Adv*., 2019, **9** 15836–15844.

51. C. Schliehe, B. H. Juarez, M. Pelletier, S. Jander, D. Greshnykh, M. Nagel, A. Meyer, S. Foerster, A. Kornowski, C. Klinke, and H. Weller, *Science*., 2010, **329**, 550-553.

52. A. B. Ghosh, N. Saha, A. Sarkar, D. N. Srivastava, P. Paul and B. Adhikary, *RSC Adv*., 2015, **5**, 102818-102827.

53. P. Abdulkin, T. L. Precht, B. R. Knappett, H.E. Skelton, D. A. Jafferson, A.E.H, Wheatley, *Part. Part. Syst. Charact.*, 2014, **31**, 571.

54. S. Mourdikoudis, and L. M. Liz-Marzan, *Chem. Mater*., 2013, **25**, 1465-1476.

View Article Online
DOI: 10.1039/D0DT01012J

Published on 05 June 2020. Downloaded by University of Exeter on 6/9/2020 8:08:14 PM.

Dalton Transactions Accepted Manuscript

55. P. Salinas-Estevane and E. M. Sa´ nchez, *Cryst. Growth Des.*, 2010, **10**, 3917-3924.

56. X. Liu, J. Chen, M. Luo, M. Leng, Z. Xia, Y. Zhou, S. Qin, D.-J. Xue, L. Lv, H. Huang, D. Niu, and J. Tang, *ACS Appl. Mater. Interfaces.*, 2014, **6**, 10687-10695.

57. B. Lu and J. Tang, *Dalton Trans*. 2014, **43**, 13948-13956.

58. A. M. Malendez, R. Arroyo and I. Gonzalez *ChemPhysChem.*, 2010, **11**, 2879 – 2886.

59. K. Gelderman, L. Lee and S.W. Donne, *J. Chem. Educ.*, 2007 **84,** 685.

60. F. Fabregat-Santiago, G. Garcia-Belmonte, J. Bisquert, P. Bogdanoff and A. Zaban, *J. Electrochem. Soc.*, 2003 **150,** E293-E298.

61. K. Darowicki, S. Krakowiak and P. Ślepski, *Electrochim. Acta.*, 2006, **51,** 2204–2208.

62. J. Satra, P. Mondal, U. K. Ghorui, and B. Adhikary, *Solar Energy Materials and Solar Cells.*, 2019, **195,** 24-33.

63. J. Zhu, X.Yan and J. Cheng, *Nanoscale Research Letters.*, 2018, **13,** 1-6.

64. X. Yu, X. Yao, T. Luo, Y. Jia, J. Liu and X. Huang, . *ACS Appl. Mater. Interfaces.*, 2014, **6**, 3689−3695.

65. D. Shi, J. Liu, R. Sun, S. Ji, S. M. Rogers, B. M. Connolly, N. Dimitratos, P. P. Wells and A. E. H. Wheatley, *Catalysis Today,* 2018, **316,** 206-213.

66. D. Y. Chung, K. J. Lee and Y. Sung, *J. Phys. Chem. C.*, 2016, **120**, 17, 9028-9035.

67. R. Zhang, C. Zhang and W. Chen, *J. Mater. Chem. A.*, 2016, **4**, 18723–18729.

View Article Online
DOI: 10.1039/D0DT01012J

Published on 05 June 2020. Downloaded by University of Exeter on 6/9/2020 8:08:14 PM.

Dalton Transactions Accepted Manuscript

68. P. Mondal, J. Satra, U. K. Ghorui, N. Saha, D. N. Srivastava and B. Adhikary, *ACS Appl. Nano Mater.*, 2018, **1**, 6015-6026.

69. J. Theerthagiri, A. P. Murthy, V. Elakkiya, S. Chandrasekaran, P. Nithyadharseni, Z. Khan, R. A. Senthil, R. Shanker, M. Raghavender, K. Parasuraman, J. Madhavan and M. Ashokkumar, *J. Industrial Eng. Chem.*, 2018, **64**, 16-59.

70. A. P. Murthy, D. Govindarajan, J. Theerthagiri, J. Madhavan and K. Parasuraman, *Electrochimica Acta.*, 2018, **283**, 1525-1533.

71. J. Theerthagiri, R. Sudha, K. Premnath, P. Arunachalam, J. Madhavan and A. M. Al-Mayouf, *Inter. J. Hydrogen Energy*., 2017, **42**, 13020–13030.

72. J. Theerthagiri, E. S. F. Cardoso, G. V. Fortunato, G. A. Casagrande, B. Senthilkumar, J. Madhavan, and G. Maia, *ACS Applied Materials & Interfaces.*, 2019, **11**, 4969–4982.

73. K. Li, Y. Li, Y. Wang, F. He, M. Jiao, H. Tang, Z. Wu, *J. Mater. Chem. A***,** 2015**, 3,** 11444-11452.

74. S. Sfaelou and P. Lianos, *AIMS Materials Science*., 2016, **3,** 270-288.

75. P. Li, Z. P. Li and B. H. Liu, *J. Power. Source*s., 2012, **199**, 146-149.

76. A. B. Ghosh, N. Saha, A. Sarkar, A. K. Dutta, J. Satra and B. Adhikary, *Dalton Trans*., 2018, **47**, 1071-1081.

77. A. B. Ghosh, N. Saha, A. Sarkar, A. K. Dutta, S. K. Maji and B. Adhikary, *New J. Chem*., 2017, **41**, 692-701.

78. T. Huang, S. Mao, G. Zhou, Z. Zhang, Z. Wen, X. Huang, S. Cib and J. Chen, *Nanoscale.,*

View Article Online

DOI: 10.1039/D0DT01012J

2015, **7**, 1301-1307.

Published on 05 June 2020. Downloaded by University of Exeter on 6/9/2020 8:08:14 PM.

Dalton Transactions Accepted Manuscript

View Article Online
DOI: 10.1039/D0DT01012J

Published on 05 June 2020. Downloaded by University of Exeter on 6/9/2020 8:08:14 PM.

Table of content entry:

Solvent tailored syntheses of two different phases of Ag_3SbS_3 nanocrystals and explored their distinctive electrochemical responses toward ORR and MOR.

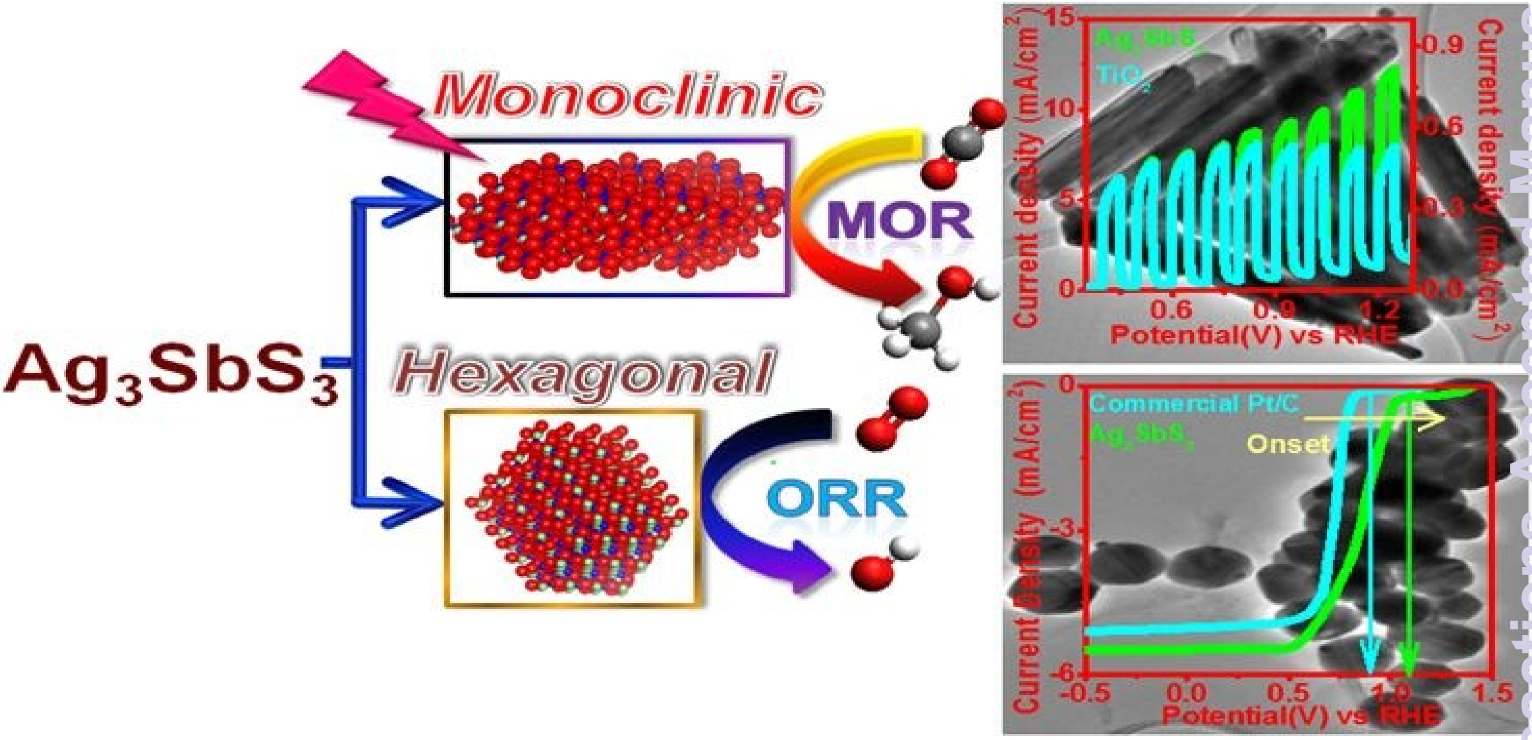

Dalton Transactions Accepted Manuscript